

BIROn - Birkbeck Institutional Research Online

Wei, F. and Prytulak, J. and Xu, J. and Wei, W. and Hammond, James O.S. and Zhao, B. (2017) The cause and source of melting for the most recent volcanism in Tibet: a combined geochemical and geophysical perspective. *Lithos* 288-9 , pp. 175-190. ISSN 0024-4937.

Downloaded from: <https://eprints.bbk.ac.uk/id/eprint/19274/>

Usage Guidelines:

Please refer to usage guidelines at <https://eprints.bbk.ac.uk/policies.html>
contact lib-eprints@bbk.ac.uk.

or alternatively

The cause and source of melting for the most recent volcanism in Tibet: a combined geochemical and geophysical perspective

Feixiang Wei^{1,2} weifeixiang@ies.ac.cn

Julie Prytulak² j.prytulak@imperial.ac.uk

Jiandong Xu¹ xujiandong@ies.ac.cn

Wei Wei¹ weiwei25011@gmail.com

James O. S. Hammond³ j.hammond@ucl.ac.uk

Bo Zhao¹ zhaobo@ies.ac.cn

¹ Key Laboratory of Active Tectonics and Volcano, Institute of Geology, China
Earthquake Administration, Beijing 100029, China.

² Department of Earth Science and Engineering, Imperial College London SW7 2AZ,
UK.

³ Department of Earth and Planetary Sciences, Birkbeck College, University of
London, London WC1E 7HX, UK.

Abstract

We investigate the youngest volcanic activity on the Tibetan Plateau by combining
observations from petrologic, geochemical and seismic tomography studies. Recent
(from 2.80 Ma to present) post-collisional potassium-rich lavas from the Ashikule

Volcanic Basin (AVB) in northwestern Tibet are characterised by remarkably enriched light rare earth elements (LREE) relative to heavy rare earth elements (HREE), and enriched large ion lithophile element (LILE) relative to high field strength elements (HFSE). Strontium and neodymium isotopic compositions are surprisingly restricted, and show little evidence for mixing or crustal contamination, despite the thick crust upon which they are erupted. Geochemical characteristics indicate a homogeneous source, highly enriched in trace elements, which is most consistent with derivation from long-lived subcontinental lithospheric mantle (SCLM). P-wave anisotropy tomography documents a gap between the north-subducting Indian slab and south-subducting Tarim slab directly beneath the AVB. We propose that volcanism in northwestern Tibet is associated with the progressive closure of this gap, during which shear heating of the SCLM can generate localised melting, with deep-seated faults providing a mechanism for erupted lavas to escape large-scale crustal contamination and fractionation in magma reservoirs. Thus, shear heating may provide an explanation for the restricted range of radiogenic isotope compositions from a SCLM source that should be, by its nature, heterogeneous on a large scale.

Key words

Tibetan Magmatism, Shoshonite. Lithospheric Mantle, Tarim Block, Shear Heating

1. Introduction

The Tibetan Plateau is the most protuberant structure on Earth, formed in

45 response to the collision of the Indian and Asian plates from 50-55 Ma ago (e.g.,
46 Royden et al., 2008; Tapponnier et al., 2001). Since the initial collision, the Indian
47 Plate has continued to subduct northward with recent studies depicting it
48 underthrusting the entire Tibetan Plateau to its northwestern margin and colliding with
49 the south-directed subducting Tarim Block (e.g., Tunini et al., 2016, Wei et al., 2015,
50 2016; Zhao et al., 2010). Collision with the Tarim block likely contributed to the rapid
51 uplift of the Tibetan Plateau at ~13 Ma (Turner et al., 1993), and resulting global
52 climate change (e.g., Kutzbach et al., 1993; Zhisheng et al., 2001).

53 A striking feature of the plateau, and northern Tibet in particular, is its widespread
54 Cenozoic post-collisional magmatism, which is distributed between 78°E and 92°E
55 and between 34°N and 36°N, forming a volcanic belt ~1300 km in length with a 100
56 km western and 400 km eastern width (e.g., Arnauad et al., 1992; Chung et al., 2005;
57 Cooper et al., 2002; Ding et al., 2003; Guo et al., 2006, 2014; Royden et al., 2008;
58 Turner et al., 1993, 1996; Wang et al., 2005; Xia et al., 2011). This volcanic belt
59 consists of more than fifty volcanic clusters that can be spatially divided into four
60 domains: (1) the Qiangtang volcanic area; (2) the Hoh Xil and middle Kunlun
61 volcanic area; (3) the west Kunlun volcanic area; (4) the Karakoram volcanic area
62 (Mo et al., 2006). The rich literature of previous studies on the post-collision lavas in
63 north Tibet shows that these Cenozoic K-rich lavas generally show remarkable
64 enrichment of LILE and LREE relative to HFSE and HREE. The petrogenesis of
65 K-rich continental lavas in Tibet, and in general worldwide, is a topic of long-standing
66 debate, with hypotheses ranging from the involvement of plumes (Guo et al., 2006),

67 crustal melting (Hacker et al., 2014; Wang et al., 2005, 2016), sub-continental
68 lithospheric mantle (Conticelli et al., 2009; Guo et al., 2015; Huang et al., 2015;
69 Turner et al., 1993, 1996; Williams et al., 2004), and contributions from subducted
70 slabs and recycled mélanges (Guo et al., 2014).

71 Temporally, magmatism in Tibet spans a period of ~45 Ma: 45-26 Ma in central
72 Tibet, 26-8 Ma in southern Tibet and 20 Ma to historic activity in northern Tibet (e.g.,
73 Guo et al., 2006, 2014; Turner et al., 1993, 1996; Williams et al., 2004; Xia et al.,
74 2011). The most recent eruption on Tibetan Plateau occurred in 1951 AD from the
75 Ashi Volcano in the Ashikule Volcanic Basin (AVB; Liu and Maimaiti, 1989; Xu et al.,
76 2012, 2014).

77 Several geophysical studies suggested that the Indian plate and Tarim Block
78 collide below the northwestern Tibetan Plateau (e.g., Tunini et al., 2016; Zhao et al.,
79 2010). However, recent tomographic studies focussed on the AVB show that the
80 volcanic basin is in fact located above a gap in the mantle lithosphere between the
81 Indian plate and Tarim Block (Wei et al., 2015, 2016; Fig. 2). The upwelling of
82 asthenospheric mantle through this gap may be responsible for the generation of the
83 Ashikule volcanoes (Fig.2; Wei et al., 2015, 2016). Because of the inaccessibility of
84 the AVB (it has an average altitude of ~4800 m and poor transport infrastructure due
85 to the sparse human population), the petrogenesis of its lavas has not been studied
86 systematically. The combined studies of Williams et al. (2004) and Guo et al. (2006,
87 2014) present some chemical analyses of nine samples from the region, but focused
88 more broadly on magmatism in the whole of northern Tibet, and thus necessarily

89 treated the limited samples from the AVB as an integrated unit. Cooper et al (2002)
90 studied the isotopic and chemical characteristics of lavas in the youngest episode,
91 which are only a part of the AVB.

92 The occurrence of present day magmatic activity and improved seismic imaging
93 allows us to combine geochemical and geophysical information. Understanding this
94 region has direct impact on evaluating hypotheses for the generation of continental
95 K-rich lavas in general and on the style and evolution of magmatism across northern
96 Tibet in particular. We present whole rock major, trace and Sr-Nd isotopic
97 compositions of 25 lavas encompassing all six volcanic episodes in the AVB
98 suggested by Liu and Maimaiti (1989) and Xu et al. (2014). In combination with
99 previous chronological data (Liu and Maimaiti, 1989; Xu et al., 2014) and
100 geophysical results (e.g., Tunini et al., 2016; Wei et al., 2015, 2016; Wittlinger et al.,
101 2004; Zhao et al., 2010), we examine the petrogenesis of recent AVB volcanism with
102 relation to its geodynamic setting.

104 2. Geological background

105 The AVB is located in the western Kunlun orogenic belt (Fig. 1), which marks the
106 northwestern margin of Tibetan Plateau (Wang et al., 2003; Wang, 2004) where the
107 Tarim Block has subducted southward, perhaps to a depth of 300 km (e.g., Tunini et
108 al., 2016; Wei et al., 2016; Wittlinger et al., 2004; Zhao et al., 2010). Structurally
109 controlled by Altyn Tagh, Karakax and Longmu-Gozha Co fault systems (Fig. 1a), the
110 AVB can be characterised as a pull-apart basin (Li et al., 2006), suffering dominantly

EW extensional stress and shearing (Furuya and Yasuda, 2011; Xu et al., 2012). The AVB is seismically active and three strong earthquakes have occurred close to this basin in 2008 (Mw 7.1), 2012 (Mw 6.2) and 2014 (Mw 6.9) (Fig. 1a; Bie and Ryder, 2014). The 2008 Yutian earthquake (Mw 7.1) ruptured a normal fault in the AVB, resulting in a surface rupture zone of up to 50 km (Bie and Ryder, 2014; Elliott et al., 2010; Furuya and Yasuda, 2011; Xu et al., 2013).

The AVB covers an area of $\sim 700 \text{ km}^2$ and encompasses 14 main volcanoes, with activity spanning from 2.80 Ma to 1951 AD (Fig. 1b). The main volcanological features in the region are volcanic cones, lava terraces and lava valleys (Xu et al., 2012). The largest and highest volcano in the basin is Dahei volcano, which has an altitude of $\sim 5090 \text{ m}$ above sea level and a relative altitude of $\sim 350 \text{ m}$. Most volcanoes in the basin are characterised by explosive eruptions (e.g., Ashi, Dahei and Wuluke volcanoes), accompanied by some effusive eruptions in the west and east of the basin (e.g., Xishan volcano and Dongshan volcanoes). Chronological studies (Liu and Maimaiti, 1989; Xu et al., 2014) show that most volcanoes were active in the Quaternary. Six episodes of volcanic activity have been defined as follows: 1. Late Ashi Episode (in 1951; Liu and Maimaiti, 1989), 2. Ashi Episode (0.12-0.17 Ma), 3. Wuluke Episode (0.20-0.29 Ma), 4. Dahei Episode (0.46-0.60 Ma), 5. Mati Episode (1.02-1.65 Ma), 6. Xi Episode (2.34-2.8 Ma).

3. Sample selection and petrography

Two field campaigns were conducted by Institute of Geology, China Earthquake

Administration in May of 2011 and 2015 where over 140 lava samples were collected. From these, twenty-five representative samples were chosen to cover the main volcanoes in the AVB according to the geological map (Fig. 1b) revised from Xu et al. (2014) and Liu and Maimaiti (1989). A thin section of each sample was made for petrographic analysis from the same material as was processed for whole-rock chemistry.

All lavas studied are porphyritic, with phenocrysts of plagioclase, clinopyroxene, orthopyroxene, phlogopite, rare olivine and Fe-Ti oxides in a ground-mass consisting of volcanic glass, plagioclase laths, clinopyroxene, orthopyroxene and rare olivine and Fe-Ti oxides (visually estimated volume percentages are presented in Table 1). The dominant phenocryst phase is plagioclase, which displays a notable lack of commonly developed zoning. All samples are vesicular, ranging from 10% to 80% by volume. A low degree of vesicular refilling by secondary minerals (calcite and clay minerals) is petrographically present in some samples (ASKL-15, ASKL-16, ASKL-17, ASKL-18, 515-1, 516-2). These obvious alteration products were removed by hand-picking the crushate before reducing the sample to powder. The phenocrysts and groundmass of analysed samples are unaltered. Figure 3 depicts representative textures encountered in the AVB lavas.

4. Methods

4.1. Major and trace element analysis

Visibly altered portions of the rocks were removed and fresh material was

reduced to centimetre size by jaw crusher. Material was then hand-picked and hand-crushed in agate mortar to fine powders for whole-rock major, trace element and Sr-Nd analysis. Whole-rock major element analysis was conducted by X-ray fluorescence (XRF) at Activation Laboratories Ltd. (Ontario, Canada; www.actlabs.com).

High-precision trace element analysis was undertaken at the Open University, UK, with an Agilent 8800 ICP-QQQ ('triple-quad' inductively coupled plasma mass spectrometer). Sample digestion was performed at the Mass Spectrometry and Geochemistry Labs at Imperial College London (MAGIC). Approximately 100 mg of rock powder was dissolved in sealed Teflon vials with a 3:1 mixture of distilled concentrated HF: HNO₃. The solutions were ultra-sonicated for 25 minutes and heated at 160 °C hot plate for at least 24 hours. They were then evaporated to near dryness and re-dissolved in 2 ml distilled 6M HCl at 120 °C for at least 24 hours. The solutions were then evaporated to complete dryness at 120 °C and re-dissolved in ~1 ml concentrated HNO₃ and evaporated at 180 °C. The last re-dissolution and evaporation step was repeated at least three times until the samples turned brownish or brown, indicating the destruction of fluorides from initial HF dissolution. Finally, 2% distilled HNO₃ was added to samples for a 1000-fold dilution.

Diluted samples were aspirated into the ICP-MS using a quartz microflow nebuliser, with an uptake rate of 0.5ml per minute, and count rates in the order of 1 – 5 x 10⁷ cps/ppm. Analyses were performed in three different collision/reaction cell modes (no gas, He, O₂ mass shift). Oxide levels (measured as CeO/Ce) were kept low,

at 1% in no gas, and 0.5% in He collision mode, and doubly charged species (Ce⁺⁺/Ce⁺) at 1.6% in no gas, and 1.2% in He collision mode. Analyses were standardised against five reference materials (digested at both the Open University and Imperial College London) that were measured at the beginning of each analytical run. The reference materials were selected on the basis of their similarity to the samples analysed, and include BIR-1, W-2, GSP-2, BHVO-2 and AGV-1. An internal standard solution (consisting of Be, Rh, In, Tm, Re, and Bi) was added to samples and run on-line throughout all analyses to correct for any instrumental drift. Drift was further monitored with a measurement block consisting of USGS reference material BIR-1 (separate digest to that used in the standardisation), a 2% HNO₃ blank, and a repeated unknown sample (ASKL-7) performed every five unknown measurements.

4.2. Sr-Nd isotopes

4.2.1. Chemical isolation of Sr and Nd

Approximately 50 mg of sample powder was leached following the method of Weis and Frey (1991, 1996) and digested using the same method as trace element digestion described above. Strontium and Nd were separated by a three-stage column chemistry. The first column employs 1.4 ml volume Bio-Rad AG50X8 200-400 mesh cation exchange resin, to separate Sr and rare earth elements (REE) from the sample matrix. Samples were loaded with 1M HCl, and the Sr fractions were collected in 4 ml 3M HCl and 0.5 ml 6M HCl. REE cuts were subsequently collected in 6.5 ml 6M HCl. The second column purifies the Sr fraction using 100 μ l shrink Teflon columns

and 100-150 mesh Eichrom Sr resin. Strontium fractions were loaded with 300 ul 3M HNO₃ and purified Sr solutions were collected with 4 ml 0.05M HNO₃. The third stage column chemistry separates Nd from the REEs using a Teflon column loaded with 1 mL of Eichrom Ln-Spec resin (100-150 um). REE cuts were loaded with 200 ul 0.2M HCl and Nd was collected in 6 ml 0.2M HCl.

4.2.2. Mass Spectrometry

Strontium and neodymium isotopic analyses were performed in the MAGIC laboratories at Imperial College London. Strontium isotopes employed a Thermo Finnigan Triton thermal ionization mass spectrometer (TIMS) whilst Nd isotope analysis used a Nu Instruments HR Multi-collector Inductively Coupled Plasma Mass Spectrometer (MC-ICPMS).

Strontium fractions were dissolved in 6M distilled HCl and loaded on single zone-refined rhenium filaments, with a TaCl₅ activator to enhance Sr ionization. Faraday cups collected masses ⁸³Kr, ⁸⁴Sr, ⁸⁵Rb, ⁸⁶Sr, and ⁸⁸Sr on channels L4, L3, L2, L1, C, and H1, respectively. Data were collected in static mode with virtual amplifier rotation, using a dummy mass of ⁸³Kr in L4. Measurement consisted of 12 blocks of 15 cycles with an electronic baseline between each block. Mass fractionation was corrected online using ⁸⁶Sr/⁸⁸Sr = 0.1194 and the exponential law. Potential contribution of ⁸⁷Rb on ⁸⁷Sr was corrected online using ⁸⁷Rb/⁸⁵Rb = 0.3856. Standard NIST SRM 987 was measured before and during measurement sessions and unknown samples were normalised to the accepted value of ⁸⁷Sr/⁸⁶Sr = 0.710248 (Thirlwall,

1991).

Neodymium fractions were re-dissolved in 0.1M HNO₃ for analysis by MC-ICPMS. Samples were introduced as 50 ppb solutions via a Nu DSN-100 Desolvation Nebuliser System. Masses ¹³⁸Ba, ¹⁴⁰Ce, ¹⁴²Nd, ¹⁴³Nd, ¹⁴⁴Nd, ¹⁴⁵Nd, ¹⁴⁶Nd, ¹⁴⁷Sm, ¹⁴⁸Nd were collected on Faraday cups L4, L3, L2, L1, C, H1, H2, H3, and H4, respectively. Measurements were collected in three blocks of 20 cycles, with an electronic baseline in between blocks. Mass fractionation was corrected using ¹⁴⁶Nd/¹⁴⁵Nd = 0.7219 and the exponential law. Neodymium standard JNdi was measured at the beginning and during the measurement session, and unknown samples were normalised according to the offset of JNdi in a single measurement session from its accepted value (¹⁴³Nd/¹⁴⁴Nd = 0.512115; Tanaka et al., 2000).

5. Results

5.1. Whole rock major and trace elements

5.1.1. Major elements

United States Geological Survey (USGS) basaltic reference materials BIR-1a and BHVO-2 were processed as unknowns for whole rock major element analyses and are in good agreement with accepted values (see supplemental information). Whole rock major element concentrations for AVB lavas are presented in Table 2. The samples yield SiO₂ contents between 45.91 and 59.48 wt%. For classification, the major element compositions were recalculated to 100% on an anhydrous basis, and plotted on the total alkali versus silica (TAS) diagram (Fig. 4a). Most samples plot within the

trachyandesite field, with several relatively old samples (ASKL-14, ASKL-17, ASKL-18, 516-11, 516-12) within the basaltic trachyandesite, phonotephrite and basanite fields. Samples greater than 2 Ma, in particular, lie at distinctly higher total alkali contents for their degree of evolution than the rest of the samples. In general, all samples are characterised by high K₂O (3.48-4.47 wt%) and K₂O/Na₂O ratios (1.08 – 1.53) (Fig. 4b), and belong to the shoshonitic series. MgO contents range from 2.24 to 7.40 wt% with Mg# of 46 to 63, displaying negative correlations with SiO₂ contents (Fig. 5a and Fig. 5b). One young sample (ASKL-3) from the recent eruption at Ashi Volcano, and 4 relatively old samples (ASKL-17, ASKL-18, 516-11, 516-12) exhibit higher MgO contents and Mg# numbers compared with other AVB samples. Given that the lavas are not co-genetic, distinct liquid lines of descent cannot be constructed. However, Fe₂O_{3(T)} (5.96-10.04 wt%) and CaO (5.15-9.39 wt%) contents display negative correlations with SiO₂, consistent in general with the fractionation of mafic phases. TiO₂ (1.36-2.22 wt%) and Al₂O₃ (12.69-14.97 wt%) have less distinct correlations with SiO₂, but support the extensive plagioclase fractionation and the presence of oxides observed in thin sections (Fig. 5; Table 1).

5.1.2. Trace elements

Trace element compositions are given in Table 2. Based on repeated analyses of sample ASKL-7 and USGS standard BIR-1a, the reproducibility of most elements was better than 2% and the measured values of standards deviate < 5% from recommended values for most elements (see supplementary information). Total

procedural blanks from digestion at MAGIC are also given in the supplemental information and are negligible compared to the concentration of elements measured.

A primitive mantle normalised incompatible element plot is presented in Fig. 6a, whilst a chondrite-normalised REE pattern is depicted in Figure 6b. Figure 6 illustrates the markedly elevated trace element concentrations of AVB lavas, consistent with K-rich continental magmatism in general. The AVB samples are all very similar in trace element composition, despite covering a range of > 2 Ma. They are characterised by significant positive Ba, Th, Pb and Nd anomalies and negative Nb, Ta, Zr and Ti anomalies. For comparison, the most isotopically enriched mantle endmember composition of “EM II” calculated for Samoan ocean island basalts (Jackson et al., 2007), global subducting sediment (GLOSS; Plank and Langmuir, 1998) and average upper continental crust (UCC, Rudnick and Gao, 2003) are also plotted. It is noteworthy that the enrichment of LILEs and LREEs in AVB lavas is more pronounced than all of the comparative suites.

The AVB lavas have $(La/Yb)_n$ ratios of 40 to 68, which correlate negatively with MgO contents (Fig. 7a) and positively with La_n (La composition normalised to primitive mantle, 131 to 295; Fig. 7b). All samples in the AVB are characterised by negative Eu anomalies ($Eu/Eu^* < 1$), which correlate positively with MgO contents, consistent with plagioclase fractionation (Fig. 7c). Titanium anomalies (Ti/Ti^*) show negative correlation with SiO_2 , consistent with oxide fractionation (Fig. 7d). Ba/Th ratios correlate negatively with Th/Nd ratios, whilst Th/La ratios show less distinct negative correlation with Sm/La ratios (Fig. 7e and Fig. 7f).

287

288 *5.2. Sr-Nd isotope geochemistry*

289 Table 3 presents Sr and Nd isotopic data for the AVB samples. USGS reference
290 materials BCR-2, BHVO-2 and BIR-1a were processed with all unknown samples and
291 are in excellent agreement with literature values (see supplemental information).
292 Despite the fresh appearance of samples in the field and the effort to exclude potential
293 alteration phase during creation of rock powders, we performed leaching tests on the
294 rock powders to exclude the effect of potential secondary alteration phases. Initial
295 tests of leached versus unleached powders showed no discernible difference in Nd
296 isotopes, but significant differences in Sr isotopes of up to 1640 ppm (see
297 supplemental information), thus all rock powders were leached according to the
298 method of Weis and Frey (1991, 1996).

299 All lavas have enriched $^{87}\text{Sr}/^{86}\text{Sr}$ (0.707490 – 0.710523) and $^{143}\text{Nd}/^{144}\text{Nd}$
300 (0.512265 – 0.512472) relative to bulk silicate earth (BSE) (Fig. 8). $^{87}\text{Sr}/^{86}\text{Sr}$ and
301 $^{143}\text{Nd}/^{144}\text{Nd}$ plot away from the bulk silicate Earth towards the enriched mantle II
302 endmember of Zindler and Hart (1986). The AVB data is remarkably restricted, with
303 two outliers belonging to the > 2 Ma lavas, which display slightly less radiogenic Sr
304 and more radiogenic Nd. Our data are in good accordance with the isotopic results of
305 younger lavas measured by TIMS (Cooper et al., 2002). Additionally, our most
306 primitive sample (ASKL-18) has similar Sr-Nd isotopic ratios to comparable literature
307 samples AH602 and AH609 of Guo et al. (2014).

308

6. Discussion

We examine the petrogenesis of the AVB lavas and attempt to link chemical and isotopic information with the unique tectonic setting as depicted by recent seismic tomography (Wei et al., 2016). First, we assess modifications to the primary lava signature. We then examine and evaluate common models for the generations of continental K-rich magmas to determine the most likely petrogenesis of the AVB lavas. Finally, we integrate recent seismic observations with geochemistry for a richer understanding of the interplay of tectonics and magma generation in the region.

6.1. Fractional crystallisation and crustal contamination

Due to the collision between the Indian and Asian plates, the thickness of the crust in northwestern Tibet has reached up to 90 km (Tunini et al., 2016; Wittlinger et al., 2004). Thus, there is ample opportunity for fractional crystallisation in crustal magma chambers and crustal assimilation to modify the chemical signature of magmas after they leave their source region(s).

Petrographic investigations of the Ashi Volcano carried out by Yu et al. (2014) proposed mixing between two crustal magma pockets based on distinct zoned phenocryst populations of pyroxene and plagioclase cores and rims. Orthopyroxene-liquid thermometry was used to estimate magmatic equilibrium temperature and pressure conditions, suggesting that an evolved magma pocket (13-18 km in depth) may connect with a deeper trachyandesite magma pocket (18-30 km in depth). Yu et al. (2014) speculated that because the two magma pockets are

vertically connected, the evolved magma pocket may be generated by fractional crystallisation of the trachyandesite magma. Beyond the petrographic analysis of Yu et al. (2014), there are only sparse reports of evolved erupted lavas in the region by Deng et al. (1998).

The impact of fractional crystallisation can be generally demonstrated in our dataset. For example, the correlations between Eu anomaly and MgO, and between Ti anomaly and SiO₂ (Fig. 7c, 7d), provide evidence for plagioclase and oxide fractionation, respectively. These phenocryst phases are also observed petrographically (Table 1). Among the younger samples, the youngest episode lavas (ASKL-3, ASKL-4 and 518-5) have the highest MgO contents, suggesting lowest degrees of fractional crystallisation. Therefore, the most recent eruption may be related to new magma inputs from the source.

With the exception of the three oldest samples (ASKL-17, ASKL-18, 516-11), Sr-Nd isotopic ratios are remarkably uniform (Fig. 8). The restricted Sr-Nd signature of the younger samples suggests a homogenous source, which is also supported by their similar trace element patterns (Fig. 6). In plots of SiO₂ versus ⁸⁷Sr/⁸⁶Sr and ¹⁴³Nd/¹⁴⁴Nd (Fig. 9a and Fig. 9b), younger samples do not show significant variation of Sr and Nd isotopes over a modest range of SiO₂ contents (53.78% to 59.48%). Therefore, despite the thick continental crust, significant crustal contamination in the younger AVB lavas are unlikely, as no correlation with SiO₂ contents are observed. It is also difficult to reconcile how crustal assimilation would produce near-identical Sr-Nd isotope compositions over million year timescales. Additionally, the LILEs and

LREEs of the AVB lavas (i.e., Rb, Sr, Sm and Nd concentrations) are significantly higher than those typically found in the continental crust (Fig. 6). Therefore, the effects of crustal assimilation are not necessarily apparent in these lavas from simple mass balance considerations. Thus, although some degree of crustal contamination seems inevitable, it is unlikely to modify the magmatic chemistry significantly.

6.2. Petrogenesis of the AVB lavas from geochemical considerations

Modification by fractional crystallisation does not affect long-lived radiogenic Sr-Nd isotope compositions and should therefore provide information about magmatic source(s). Guo et al. (2014) proposed that post-collisional K-rich magmatism in northern Tibet reflects subduction-related metamorphic mélanges. They suggested mélange zones on top of both the Indian and Tarim subducting slabs mix slab materials and mantle rocks. These mixed mélanges are fluid-rich and thus buoyant, and subsequently upwell and partially melt to high degrees. This model does not include a means of focussing volcanism and explicitly involves materials with a range of isotope compositions. For example, the Indian and Tarim slabs are isotopically distinct (Tarim block, $^{87}\text{Sr}/^{86}\text{Sr} \approx 0.708$ and $^{143}\text{Nd}/^{144}\text{Nd} \approx 0.5119$; Indian plate, $^{87}\text{Sr}/^{86}\text{Sr} > 0.713$ and $^{143}\text{Nd}/^{144}\text{Nd} < 0.5122$; Guo et al., 2014) and a wide range of radiogenic isotope variability is possible when considering the inaccessible sedimentary package that these slabs may host.

According to the spatial classification in Guo et al. (2014), the AVB belongs to the middle sub-group volcanic field, which displays variable mixing proportions of

the Indian and Tarim materials. The Sr-Nd isotopic signatures of the AVB lavas are extremely restricted (Fig. 8, 9), and do not conform to the notion of three endmember-mixtures (DMM, Tarim and Indian mélanges). Marschall and Schumacher (2012) proposed a ‘mélange average’ to highlight trace element similarities with arc volcanism. Even though the AVB lavas share similar characteristics of distinct enrichment in Pb and depletion in Nb, Ta and Ti, mélange abundances of LILEs and LREEs are much lower than those of the AVB lavas and the slope of the REE is markedly flatter in mélange averages compared to the AVB lavas. Although we cannot definitively rule out a small contribution from mélanges, they are highly unlikely to dominate the chemical signature of AVB lavas.

Tomographic images (Fig. 2) depict a low-velocity gap between the Indian and Tarim lithospheres, which may be a channel for upwelling asthenosphere (Wei et al., 2015, 2016). Derivation solely from a shallow asthenospheric, MORB-like source is inconsistent with isotopic (Fig. 8) and trace element (Fig. 6b) signatures of the AVB. The elevated trace element concentrations of AVB lavas, and K-rich continental lavas in general, require a source enriched beyond fertile primitive mantle. Given the thick, enriched continental crust in the region, it may provide such a source. Volcanism related to crustal melting has been reported in the Hohxil area of northern Tibet by Wang et al. (2005), but the K-rich “adakitic” volcanic rocks in this area exhibit high SiO₂ contents (61-67%). The major element features of the AVB lavas, such as their low SiO₂ contents (Fig. 4, 5) make it unlikely that they are derived by direct partial melting of continental crust. High source concentrations of trace elements can also be

397 achieved by multistage enrichments by small degree melt metasomatism of
398 underlying lithosphere. Indeed, partial melting of the metasomatised sub-continental
399 lithospheric mantle (SCLM) has often been invoked for potassic magmatism in Tibet
400 (e.g., Cooper et al., 2002; Turner et al., 1993, 1996; Williams et al., 2004) and the
401 western Mediterranean (e.g., Conticelli et al., 2009).

402 At face value, melting of the metasomatised SCLM appears to offer the best
403 explanation for the chemical characteristics of the AVB lavas. The depth of melt
404 generation can be explored using the REE and HFSE characteristics. Williams et al.
405 (2004) compared the difference between peridotite melting models of both spinel and
406 garnet facies. They suggested that partial melting of a spinel-facies
407 phlogopite-bearing peridotite source was responsible for the volcanism in north Tibet.
408 However, as the authors explained, their model cannot reproduce reasonable
409 concentrations of yttrium, a HREE. Additionally, spinel-facies sources are
410 inconsistent with the absence of Zr/Hf fractionation in our AVB samples (46.7-51.9;
411 Fig. 10). Fractionation is expected, because D_{Zr}/D_{Hf} in garnet facies is around one,
412 whilst D_{Zr}/D_{Hf} of clinopyroxene in spinel stability field is around 0.5 (Weyer et al.,
413 2003), thus different degrees of partial melting in the spinel stability field would cause
414 variable Zr/Hf ratios.

415 Trace element geochemistry can also provide clues about the mineralogy of the
416 mantle source. For example, Nb-Ta, are chemical twins, having the same valency (+5)
417 and similar ionic radii, thus, they are expected to behave congruently in both fluids
418 and melts (e.g., Dostal and Chatterjee, 2000; Kalfoun et al., 2002; Weyer et al., 2003).

In Fig. 10, the AVB lavas display variable Nb/Ta ratios, significantly higher than the primitive mantle (PM), UCC, GLOSS and EM2 endmembers. Depleted Nb-Ta concentrations and high Nb/Ta ratios of the AVB lavas may be related to Ti-rich oxide minerals in the residual phases such as rutile, amphibole and phlogopite. Xenolith data from Kalfoun et al. (2002) indicate that rutile may be an important host for HFSE, which is consistent with the HFSE depletions (such as Nb, Ta, Zr and Hf) and low Ti_2O content in the AVB lavas. Other alternative residual minerals are amphibole and phlogopite, which are the only Nb- and Ta-rich silicate minerals in the upper mantle (Kalfoun et al., 2002).

The existence of phlogopite in the upper mantle has long been demonstrated by petrological studies (e.g., Kushiro et al., 1968; Sudo and Tatsumi, 1990; Wyllie and Sekine, 1982). In Fig. 4, K_2O contents are high, but similar (3.48-4.47 wt%) over a comparatively wide range of SiO_2 (45.91-59.48%). In combination with the relatively low MgO contents of the AVB lavas, these characteristics indicate buffering of K_2O by potassium-rich phases in the mantle source (i.e., phlogopite and/or amphibole). Because Rb and Ba are compatible in phlogopite, whilst Rb, Sr and Ba are moderately compatible in amphibole, melts in equilibrium with phlogopite have high Rb/Sr and lower Ba/Rb ratios than that formed in amphibole-bearing source. As suggested by Furman and Graham (1999) and Yang et al. (2004), samples with low Ba/Rb (<20) and high Rb/Sr (>0.1) are generally derived from phlogopite-bearing source. In Fig. 11, the plot of Rb/Sr versus Ba/Rb ratios implies that the AVB lavas are derived from a phlogopite-rich source.

The ~90 km-thick crust (Tunini et al., 2016; Wittlinger et al., 2004) suggests that the SCLM is deep with high temperature and pressure. Phlogopite is more stable than amphibole at these P-T conditions (Condamine and Medard, 2014; Sudo and Tatsumi, 1990). Therefore, we suggest that the AVB lavas are likely derived by partial melting of the Tibetan phlogopite-garnet-bearing SCLM. This result is in accordance with melting experiments conducted by Condamine et al. (2016), which suggest that worldwide post-collisional K-rich lavas are generated by melting of metasomatised phlogopite-bearing garnet-peridotite. The three oldest samples (ASKL-17, ASKL-18, 516-11) exhibit the most mafic major element characteristics in our dataset. They are distinct, with Sr-Nd isotope compositions slightly less enriched than the younger lavas of the dataset (Fig. 8). The oldest two samples are also geographically located to the northwest of the main AVB (Fig. 1). They likely have a slightly different petrogenetic history, however, we envision a similar process of melting phlogopite-garnet-bearing SCLM.

It is an interesting question as to how such an isotopically homogeneous signature can be generated from the SCLM, which should be highly heterogeneous given its long-term enrichment by multiple metasomatic events. Initial metasomatic events of the Tibetan lithosphere may have begun as early as the Proterozoic when the Proto-Tethys lithosphere subducted beneath the basement of Tibet, and continued until the Late Triassic with the closure of Paleo-Tethys Ocean (Jiang et al., 2013; Mattern and Schneider, 2000; Pullen et al., 2008; Sone and Metcalfe, 2008). The impacts of Tethyan oceanic lithosphere on Tibetan lithosphere have been

demonstrated by several studies of Cenozoic volcanism (e.g., Chung et al., 2005; Ding et al., 2003).

Generally, Nb-Ta-Ti negative anomalies in igneous rocks are indicators of subduction (Briqueu et al., 1984; Foley et al., 1999). However, contemporary subduction of the Indian plate is unlikely to result in homogeneous metasomatism of the entire Tibetan lithosphere (Guo et al., 2006; Turner et al., 1996; Williams et al., 2004). The metasomatised upper mantle in the plateau is likely to be associated with slab-derived components such as ancient subducting sediments, which may originate from Proto-Tethys and Paleo-Tethys oceanic lithospheres.

The petrogenesis of AVB discussed above is in accordance with most shoshonites of the world, such as western Alps (Conticelli et al., 2009), Fiji (Leslie et al., 2009), Izu-Bonin-Mariana intra-oceanic arc (Ishizuka et al., 2010; Sun and Stern, 2001) and Aeolian (Peccerillo et al., 2013). They are generally generated by partial melting of an enriched mantle and display similar geochemical characteristics, including enrichment in LILE and depletion in Nb-Ta-Ti. However, tectonic mechanisms for partial melting of enriched mantles are diverse. The majority of shoshonitic magmatism is generated in three broad tectonic settings (Gill et al., 2004): (1) post-collisional orogens, e.g. Tibet (Turner et al., 1996) and the Alps (Conticelli et al., 2009); (2) rifting in continental post-subduction areas and continental magmatic arcs, e.g. Cascades (Conrey et al., 1997); (3) intra-ocean island arc settings, e.g. Fiji (Leslie et al., 2009) and Izu-Bonin-Mariana arc (Ishikuka et al., 2010; Sun and Stern, 2001). Shoshonitic rocks in the former two tectonic settings are mainly characterised by Ce/Yb ratios

higher than 46.5 and oceanic-arc related shoshonitic rocks display Ce/Yb ratios lower than 46.5 (Gill et al., 2004). The Ce/Yb ratios of AVB lavas range from 114 to 191, which is consistent with the post-collisional settings. Due to the complicated tectonic setting of the AVB and the multiple possible contributors to their chemical budget (e.g., subduction package of both Indian and Tarim slabs), a combined geophysical and geochemical perspective may yield more insight to the triggering mechanism for partial melting of the enriched SCLM.

6.3. Integrated Geophysical and Geochemical views

The historic volcanic activity in the AVB allows us to combine present day seismic images of the region with geochemistry. There are four competing geodynamical models for the petrogenesis of the volcanism in northwestern Tibet: (1) convective removal of the lower part of lithosphere (e.g., Chung et al., 2005; Turner et al., 1993, 1996; Williams et al., 2004; Xia et al., 2011); (2) mixing of Indian and Tarim mélanges (Guo et al., 2014); (3) addition of subduction components without mélanges (e.g., Arnaud et al., 1992; Ding et al., 2003; Tapponnier et al., 2001); and (4) upwelling asthenosphere (Wei et al., 2015, 2016). Here we have the unique opportunity to investigate which of these scenarios is most consistent with both geochemical and geophysical constraints.

6.3.1. Convective removal of the lower part of lithosphere

Several previous studies highlight the possibility of partial melting of the SCLM

507 by convective removal of the lower part of lithosphere (e.g., Chung et al., 2005;
508 Cooper et al., 2002; Turner et al., 1993, 1996; Williams et al., 2004; Xia et al., 2011).
509 According to these geochemical studies, after the primary collision at 50-55 Ma,
510 under the squeezing pressure of the north-subducting Indian plate and the resisting
511 Tarim Block, the northwest Tibet lithosphere started to shorten and thicken to twice its
512 original thickness, accompanied by the fast uplift of the Tibetan Plateau. Subsequently,
513 owing to gravitational instability and asthenospheric heating, the lower part of the
514 Tibetan lithosphere was convectively removed. Thinning of the lithosphere led to the
515 upwelling of asthenosphere, which caused partial melting of the Tibetan SCLM. An
516 important piece of evidence for this model is that no young volcanism has been found
517 in southern Tibet after the southern Tibetan lithosphere was underthrust by the cold
518 Indian Plate at ~10 Ma, which shut down the asthenospheric source (Chung et al.,
519 2005; Xia et al., 2011).

520 This model can explain the petrogenesis of the K-rich volcanic rocks and their
521 trace element enrichment. However, it requires the existence of K-rich layer in the
522 Tibetan lithosphere. Even if it is true, it is still difficult to explain the coincidence of
523 wide exposure of K-rich volcanism on the whole Tibetan Plateau, which indicates that
524 volcanism only happens when the lithosphere is thinned to this K-rich layer. In
525 addition, if the magmatism of AVB is associated with removal of the lower part of
526 lithosphere, the sinking of the delaminated cold lithosphere would decrease the
527 temperature of the asthenosphere beneath the AVB. However, tomographic images
528 (Fig. 2) in this region do not show a fast seismic anomaly expected for delaminated

lithosphere, although such a feature could be below the resolution of the seismic models (~50 km, Wei et al., 2016).

6.3.2. Mélange melting

As discussed, the mélange model proposed by Guo et al. (2014) is inconsistent with the radiogenic isotopic homogeneity we document in AVB lavas. The mélange-melting model is also inconsistent with the following geophysical observations: (1) Recent seismic results do not support the steep subduction of Indian plate beneath the AVB (Fig. 2; Tunini et al., 2016; Wei et al., 2015, 2016; Zhao et al., 2010). Steep subduction of the Indian plate is only observed on the west (Pamir-Hindu Kush region; Negredo et al., 2007) and east of Tarim basin (south of Qaidam Basin; Li et al., 2008; Zhao et al., 2010). (2) Because the Indian plate has subducted more than 600 km beneath the Tibet, it is unclear how the Indian plate is able to dehydrate and specifically focus volcanism in the AVB.

6.3.3. Subduction components without mélange assemblages

From south to north, the Tibetan Plateau consists of four roughly east-west-trending terranes: Lhasa, Qiangtang, Songpan-Ganzi and Kunlun (Dewey, 1988). Tectonic studies suggest that volcanism on the Tibetan Plateau may be associated with the subduction of Indian and Asian plates (e.g., Arnaud et al., 1992; Ding et al., 2003; Tapponnier et al., 2001). Specifically, in northwestern Tibet, the AVB lavas may be generated by the subduction of Indian and Tarim slabs. This

subduction model is supported by field observations, such as the East-west-trending K-rich volcanic belts.

However, Cenozoic volcanism on the Tibetan Plateau does not display a pattern of stepwise subduction of continental lithosphere (e.g., Guo et al., 2006; Williams et al., 2004). Moreover, this large-scale subduction model is inconsistent with recent seismic studies. For example, large-scale subduction of Asian lithospheres would result in an uneven base to the Tibetan lithosphere, which is not observed (Fig. 2; Wei et al., 2015, 2016; Zhao et al., 2010). Though the existence of the subducting Tarim Block beneath northwestern Tibet is well-documented (e.g., Wei et al., 2015, 2016; Wittlinger et al., 2004, Zhao et al., 2010), the impacts of Tarim Block on northwestern magmatism may be minor, as plate subduction would cause an increase in age of the northwestern magmatism from north to south, which are not observed (Guo et al., 2006, 2014).

6.3.4. Asthenosphere Upwelling and Shear Heating

Wei et al. (2015; 2016) performed high resolution (1°) P-wave velocity tomography beneath the AVB. They revealed a mantle lithospheric between the Indian and Tarim slabs directly beneath the AVB, and suggested that the volcanism is associated with the upwelling of the asthenosphere. These models show that in northwestern Tibet, the Indian and Tarim LABs are visible in seismic tomography with fast seismic velocities extending to depths of approximately 250 km (Figure 2), which is in accordance with the results of Zhao et al. (2010). The upper boundaries

between the subducting slabs and Tibetan lithosphere are not observed, suggesting that the lithosphere of the subducting slabs and the Tibetan lithosphere may have integrated into one thick lithosphere.

However, some lateral variations exist in lithospheric structure. The continuous fast seismic velocities in the west vertical cross section (80°E) of P-wave tomography indicates that the Indian and Tarim slabs have collided with each other. However, the middle vertical cross section (81.58°E , on the AVB) show discontinuous fast seismic velocities suggesting that the north edge of Indian plate has not yet collided with the Tarim Block, thus there exists a gap ~ 120 km wide between the two slabs directly beneath the AVB; the east vertical cross section (83°E) shows a larger gap between those two slabs. This discontinuous lithospheric structure is supported by a recent joint analysis of seismic velocity, gravity and topography in the Tarim Basin and surrounding region (Deng et al., 2017) showing that the AVB is underlain by weak, low-density material compared to the thick, dense and strong Tarim block to the north. Owing to the limited number of seismic stations in the sparsely populated region, it is hard to constrain the details of this, but Deng et al. (2017) suggest that the mantle in this region is anomalously buoyant. They argue that the region is too narrow to be caused by a thermal anomaly and suggest a compositional anomaly (e.g., metamorphism linked to subduction fluids) or a localised heat source (e.g., shear-heating) are likely mechanisms to weaken the lithosphere.

Global positioning system measurements indicate that the convergence rate between India and Tarim Basin in the direction of relative motion between India and

Eurasia (\sim N20°E) (Sella et al., 2002) is \sim 28 mm/year (Zhang et al., 2004). As a result, the upper mantle in the gap between the Indian and Tarim lithospheres is being squeezed by the relative motion of the two subducting lithospheres. Since we have excluded the models of convective removal of the SCLM, subduction and *mélange* melting, we speculate that partial melting of the SCLM is likely related to shear heating and/or upwelling of asthenosphere in the upper mantle. Since a significant chemical signature of asthenosphere has not been detected in this study, we suggest that the heat contribution of shear heating may be dominant.

Convergence of lithospheres may result in viscous strain-rate melting in the upper mantle (Kincaid and Silver, 1996), which can provide the heat for partial melting of the SCLM without removing of the lower part of the SCLM. Furthermore, shear heating can cause very localised heating in the lithosphere close to large faults (Leloup et al. 1999) providing a possible explanation for the near invariant radiogenic isotope signature derived from the SCLM, which should be heterogeneous on a large scale. The duration of this viscous heating is thought to be short, spanning a period of \sim 12-15 Ma (Kincaid and Silver, 1996), which is consistent with the age of northwestern volcanism (8.27 Ma to present; Cooper et al., 2002; Guo et al., 2016, 2014; Turner et al., 1993; 1996; Williams et al., 2004).

Shear heating has been invoked as a mechanism for crustal magmatism, with recent models suggesting that shear heating coupled with the insulating nature of hot rocks provides an efficient mechanism for melting in orogenic belts (e.g., Whittington et al., 2009). For example, leucogranites on an active thrust in the Himalayas have

617 been proposed to result from partial melting triggered by shear-heating (Harrison et al.,
618 1997, 1998) as well as in other orogens (e.g., Trans-Hudson, Appalachain, Nabalek
619 and Liu, 2004). In the AVB, the Altyn Tagh fault extends down to a depth of 140 km
620 with strike-slip shear in the SCLM (Wittlinger et al., 1998), thus it is possible that
621 shear heating in the SCLM precedes shoshonitic melt generation. Once melts are
622 formed, the deep-seated lithospheric faults may allow melt to migrate to the Earth
623 surface, resulting in minimal crustal contamination of the primary magma.

624 If our model that the northwestern volcanism is related to the mantle gap between
625 the two subducting slabs is correct, the closure of the gap in the west prior to the east
626 should result in older lavas in the west. As suggested by seismic images (Fig. 2), there
627 must be a critical point between 80°E and 81.56°E, where the Indian slab has just
628 collided with the Tarim slab. Tomographic results based on the model of Wei et al.,
629 (2016) suggest that this critical point is located at ~81°E. To the west of 81°E, the gap
630 between the two slabs closed prior to the east, thus the volcanism related to the gap
631 are chronologically older than the volcanism in the east. This chronological difference
632 is in accordance with the ages of northwestern volcanism summarised by Guo et al.
633 (2014). To the west of 81°E, the average ages of Tianshuihai, Quanshuigou,
634 Qitaidaban, Dahongliutan and Kangxiwa lavas are 5.20, 5.23, 8.27, 3.78, 3.24 Ma,
635 respectively (Fig. 12). In the east of 81°E, the average age of Ashikule, Keliya, Pulu
636 and Heishibei are 1.07, 0.56, 1.20 and 1.28 Ma, respectively, which are significantly
637 younger than those of the western volcanic fields (Fig. 12). Additionally, as strong
638 tectonic activities are usually manifested geomorphologically, we speculate that the

formation of arc-shape Kegang fault may also be related to the closure of the lithospheric gap (Fig. 1, Fig. 12).

7. Summary and Outlook

New geochemical analyses of the most recent volcanism in Tibet are combined with recent tomographic studies beneath the AVB at the northwestern margin of the Tibetan Plateau. We suggest that AVB lavas are most likely generated by partial melting of the Tibetan phlogopite-bearing SCLM within the garnet stability field. While the resolution of the seismic models alone cannot distinguish the mechanism of heat generation, the homogeneous characteristics of the radiogenic isotope signatures point to a very localised source. This argues against a broad asthenospheric upwelling or direct link with subduction-derived fluids or chemically heterogeneous *mélange* contributions. Rather, we suggest heat is provided via localised shear-heating along lithospheric faults accommodating the closure of the Indian and Tarim slabs. This mechanism, as well as explaining the seismic and radiogenic isotope signatures, provides a viable means of transport to account for the lack of crustal contamination in the samples. This model suggests that evolving volcanism in Tibet, and possibly in other transpressive regimes, are more directly linked to the evolution of large-scale lithospheric faults as opposed to the subduction of the Indian and Tarim slabs. More precise dating of tectonic and volcanic activity, more concentrated geochemical study and improved geophysical imaging are required to fully test this hypothesis.

Acknowledgements

We thank S. Turner and an anonymous reviewer for their constructive comments and suggestions that helped us greatly to improve the manuscript. We are grateful to B. Coles and K. Kreissig for their great help of the MAGIC mass spectrometry and chemistry training. We thank S. Hammond (Open University) for precise trace element analyses. This work was funded by the National Natural Science Foundation of China (Grant 41372344) and a China Scholarship Council (CSC) award to FW for his visit to MAGIC.

References

Arnaud, N.O., Vidal, Ph., Tapponnier, P., Matte, Ph., Deng, W.M., 1992. The high K₂O volcanism of northwestern Tibet: Geochemistry and tectonic implications. *Earth and Planetary Science Letters* 111, 351-367.

Bie, L., Ryder, I., 2014. Recent seismic and aseismic activity in the Ashikule stepover zone, NW Tibet. *Geophysical Journal International* 198, 1632-1643.

Bouvier, A., Vervoort, J.D., Patchett, P.J., 2008. The Lu-Hf and Sm-Nd isotopic composition of CHUR: Constraints from unequilibrated chondrites and implications for the bulk composition of terrestrial planets. *Earth and Planetary Science Letters* 273, 48-57.

683 Briquieu, L., Bougault, H., Joron, J.L., 1984. Quantification of Nb, Ta, Ti and V
684 anomalies in magmas associated with subduction zones: petrogenetic implications.
685 Earth and Planetary Science Letters 68, 297-308.

686

687 Chung, S.L., Chu, M.F., Zhang, Y., Xie, Y., Xie, Y., Lo, C.H., Lee, T.Y., Lan, C.Y., Li,
688 X., Zhang, Q., Wang, Y., 2005. Tibetan tectonic evolution inferred from spatial and
689 temporal variation in post-collisional magmatism. Earth Science Reviews 68,
690 173-196.

691

692 Condamine, P., Medard, E., 2014. Experimental melting of phlogopite-bearing mantle
693 at 1 GPa: Implication for potassic magmatism. Earth and Planetary Science Letters
694 397, 80-92.

695

696 Condamine, P., Medard, E., Devidal, J.L., 2016. Experimental melting of
697 phlogopite-peridotite in the garnet stability field. Contributions to Mineralogy and
698 Petrology 171, 95.

699

700 Conrey, R.M., Sherrod, D.R., Hooper, P.R., Swanson, D.A., 1997. Diverse primitive
701 magmas in the Cascade arc, northern Oregon and southern Washington. Canadian
702 Mineralogist 35, 367-397.

703

704 Conticelli, S., Guarnieri, L., Farinelli, A., Mattei, M., Avanzinelli, R., Bianchini, G.,

705 Boari, E., Tommasini, S., Tiepolo, M., Prelevic, D., Venturelli, G., 2009. Trace
706 elements and Sr-Nd-Pb isotopes of K-rich, shoshonitic, and calc-alkaline magmatism
707 of the Western Mediterranean Region: Genesis of ultrapotassic to calc-alkaline
708 magmatic associations in a post-collisional geodynamic setting. *Lithos* 107, 68-92.
709

710 Cooper, K.M., Reid, M.R., Dunbar, N.W., McIntosh, W.C., 2002. Origin of mafic
711 magmas beneath northwestern Tibet: Constraints from ^{230}Th - ^{238}U disequilibria.
712 *Geochemistry, Geophysics, Geosystems* 3(11), 1-23.
713

714 Deng, W.M., 1998. Cenozoic Intraplate Volcanic Rocks in the Northern
715 Qinghai-Xizang Plateau. Geological Publishing House, Beijing p. 180 (in Chinese
716 with English abstract).
717

718 Deng, Y., Levandowski, W., & Kusky, T., 2017. Lithospheric density structure
719 beneath the Tarim basin and surroundings, northwestern China, from the joint
720 inversion of gravity and topography. *Earth and Planetary Science Letters* 460,
721 244–254.
722

723 Dewey, J.F., 1988. Extensional collapse of orogens. *Tectonics* 6, 1123-1139.
724

725 Ding, L., Kapp, P., Zhong, D., Deng, W., 2003. Cenozoic volcanism in Tibet:
726 Evidence for a transition from oceanic to continental subduction. *Journal of Petrology*

727 44(10), 1833-1865.

728

729 Dostal, J., Chatterjee, A.K., 2000. Contrasting behavior of Nb/Ta and Zr/Hf ratios in a
730 peraluminous granitic pluton (Nova Scotia, Canada). *Chemical Geology* 163,
731 207-218.

732

733 Elliott, J.R., Walter, R.J., England, P.C., Jackson, J.A., Li, Z., 2010. Parsons, B.,
734 Extension on the Tibetan plateau: recent normal faulting measured by InSAR and
735 body wave seismology. *Geophysical Journal International* 183, 503-535.

736

737 Foley, S.F., Barth, M.G., Jenner, G.A., 1999. Rutile/melt partition coefficients for
738 trace elements and an assessment of the influence of rutile on the trace element
739 characteristics of subduction zone magmas. *Geochimica et Cosmochimica Acta* 64(5),
740 933-938.

741

742 Furman, T., Graham, D., 1999. Erosion of lithospheric mantle beneath the East
743 African Rift system: geochemical evidence from the Kivu volcanic province. *Lithos*
744 48, 237-262.

745

746 Furuya, M., Yasuda, T., 2011. The 2008 Yutian normal faulting earthquake (Mw 7.1),
747 NW Tibet: Non-planar fault modelling and implications for the Karakax Fault.
748 *Tectonophysics* 511(3), 125-133.

749

750 Gill, R.C.O., Aparicio, A., Azzouzi, M.El., Hernandez, J., Thirlwall, M.F., Bourgois, J.,
751 Marriner, G.F., 2004. Depleted arc volcanism in the Alboran Sea and shoshonitic
752 volcanism in Morocco: geochemical and isotopic constrains on Neogene tectonic
753 processes. *Lithos* 78, 363-388.

754

755 Guo. Z., Wilson, M., Liu, J., Mao, Q., 2006. Post-collisional, potassic and
756 ultrapotassic magmatism of the northern Tibetan Plateau: Constraints on
757 characteristics of the mantle source, geodynamic setting and uplift mechanisms.
758 *Journal of Petrology* 47(6), 1177-1220.

759

760 Guo, Z., Wilson, M., Zhang, L., Zhang, M., Cheng, Z., Liu, J., 2014. The role of
761 subduction channel mélanges and convergent subduction systems in the petrogenesis
762 of post-collisional K-rich mafic magmatism in NW Tibet. *Lithos* 198-199, 184-201.

763

764 Guo, Z., Wilson, M., Zhang, M., Cheng, Z., Zhang, L., 2015. Post-collisional
765 ultrapotassic mafic magmatism in south Tibet: Products of partial melting of
766 pyroxenite in the mantle wedge induced by roll-back and delamination of the
767 subducted Indian continental lithosphere slab. *Journal of Petrology* 56(7), 1365-1406.

768

769 Hacker, B.R., Ritzwoller, M.H., Xie, J., 2014. Partially melted, mica-bearing crust in
770 Central Tibet. *Tectonics* 33(7), 1408-1424.

771

772 Harrison, T.M., Lovera O.M., Grove, M., 1997. New insights into the origin of two
773 contrasting Himalayan granite belts. *Geology* 25(10), 899-902.

774

775 Harrison, T.M., Grove, M., Lovera O.M., Caltos, E.J., 1998. A model for the origin of
776 Himalayan anataxis and inverted metamorphism. *Journal of Geophysical Research*
777 103(B11), 27017-27032.

778

779 Huang, F., Chen, J.L., Xu, J.F., Wang, B.D., Li, J., 2015. Os-Nd-Sr isotopes in
780 Miocene ultrapotassic rocks of southern Tibet: Partial melting of a pyroxenite-bearing
781 lithospheric mantle. *Geochimica et Cosmochimica Acta* 163, 279-298.

782

783 Ishizuka, O., Yuasa, M., Tamura, Y., Shukuno, H., Stern, R.J., Naka, J., Joshima, M.,
784 Taylor, R.N., 2010. Migrating shoshonitic Magmatism tracks Izu-Bonin-Mariana
785 intra-oceanic arc rift propagation. *Earth and Planetary Science Letters* 294, 111-122.

786

787 Jackson, M.G., Hart, S.R., Kopperss, A.P., Staudigel, H., Konter, J., Blusztajn, J.,
788 Kurz, M., Russell, J., 2007. The return of subducted continental crust in Samoan lavas.
789 *Nature* 448, 684-687.

790

791 Jiang, Y.H., Jia, R.Y., Liu, Z., Liao, S.Y., Zhao, P., Zhou, Q., 2013. Origin of Middle
792 Trissic high-K calc-alkaline granitoids and their potassic microgranular enclaves from

793 the western Kunlun orogeny, northwest China: A record of the closure of Paleo-Tethys.
794 *Lithos* 156-159, 13-30.
795
796 Kalfoun, F., Ionov, D., Merlet, C., 2002. HFSE residence and Nb/Ta ratios in
797 metasomatised, rutile-bearing mantle peridotites. *Earth and Planetary Science Letters*
798 199, 49-65.
799
800 Kincaid, C., Silver, P., 1996. The role of viscous dissipation in the orogenic process.
801 *Earth and Planetary Science Letters* 142, 271-288.
802
803 Kushiro, I., Syono, Y., Akimoto, S.I., 1968. Stability of phlogopite at high pressures
804 and possible presence of phlogopite in the Earth's upper mantle. *Earth and Planetary*
805 *Science Letters* 3, 197-203.
806
807 Kutzbach, J.E., Prell, W.L., Ruddiman, W.F., 1993. Sensitivity of Eurasian climate to
808 surface uplift of the Tibetan Plateau. *The Journal of Geology* 101, 177-190.
809
810 Le Bas, M.J., Le Maitre, L.E., Streckeisen, A., Zanettin, B., 1986. A chemical
811 classification of volcanic rocks based on the total alkali-silica diagram. *Journal of*
812 *Petrology* 27(3), 745-750.
813
814 Leloup, P. H., Ricard, Y., Battaglia, J. and Lacassin, R., 1999. Shear heating in

815 continental strike-slip shear zones: model and field examples. *Geophysical Journal*
816 International, 136, 19-40.

817

818 Leslie, R.A.J., Danyushevsky, L.V., Crawford, A.J., Verbeeten, A.C., 2009. Primitive
819 shoshonites from Fiji: Geochemistry and source components. *Geochemistry,*
820 *Geophysics, Geosystems* 10(7).

821

822 Li, C., van der Hilst, R.D., Meltzer, A.S., Engdahl, E.R., 2008. Subduction of the
823 Indian lithosphere beneath the Tibetan Plateau. *Earth and Planetary Science Letters*
824 274, 157-168.

825

826 Li, H.B., Yang, J.S., Xu, Z.Q., Sun, Z.M., Tapponnier, P., van der Woerd, J., Meriaux,
827 A.S., 2006. The constraint of the Altyn Tagh fault system to the growth and rise of the
828 northern Tibetan plateau, *Earth Science Frontiers* 13(4), 59-79 (in Chinese with
829 English Abstract).

830

831 Liu, J., Maimaiti, Y., 1989. Distribution and ages of Ashikule volcanoes on the West
832 Kunlun Mountains, west China. *Bulletin of Glacier Research* 7, 187-190.

833

834 Marschall, H.R., Schumacher, J.C., 2012. Arc magmas sourced from mélange dispirs
835 in subduction zones. *Nature Geoscience* 5, 862-867.

836

837 Mattern, F., Schneider, W., 2000. Suturing of the Proto- and Paleo-Tethys oceans in
838 the western Kunlun (Xinjiang, China). *Journal of Asian Earth Sciences* 18, 637-650.
839

840 Miller, C., Schuster, R., Klotzli, U., Frank, W., Purtscheller, F., 1999. Post-collisional
841 Potassic and ultrapotassic magmatism in SW Tibet: Geochemical and Sr-Nd-Pb-O
842 isotopic constraints for mantle source characteristics and petrogenesis. *Journal of*
843 *Petrology* 40(9), 1399-1424.
844

845 Mo, X., Zhao, Z., Deng, J., Flower, M., Yu, X., Luo, Z., Li, Y., Zhou, S., Dong, G.,
846 Zhu, D., Wang, L., 2006. Petrology and geochemistry of postcollisional volcanic
847 rocks from the Tibetan plateau: Implications for lithosphere heterogeneity and
848 collision-induced asthenospheric mantle flow. *Geological Society of America Special*
849 *Papers* 409: 507-530.
850

851 Nabelek, P.I., Liu, M., 2004. Petrologic and thermal constraints on the origin of
852 leucogranites in collisional orogens. *Geological Society of America Special Papers*
853 398, 73-85.
854

855 Negredo, A.M., Replumaz, A., Villasenor, A., Guillot, S., 2007. Modeling the
856 evolution of continental subduction processes in the Pamir-Hindu Kush region. *Earth*
857 *and Planetary Science Letters* 259, 212-225.
858

859 Peccerillo, A., De Astis, G., Faraone, D., Forni, F., Frezzotti, M.L., 2013.
860 Compositional variations of magmas in the Aeolian arc: implications for petrogenesis
861 and geodynamics. Geological Society, London, Memoirs 37, 491-510.
862

863 Plank, T., Langmuir, C.H., 1998. The chemical composition of subducting sediment
864 and its consequences for the crust and mantle. Chemical Geology 145, 325-394.
865

866 Pullen, A., Kapp, P., Gehrels, G.E., Vervoort, J.D., Ding, L., 2008. Triassic continental
867 subduction in central Tibet and Mediterranean-style closure of the Paleo-Tethys
868 Ocean. Geology 36(5), 351-354.
869

870 Royden, L.H., Burchfiel, B.C., van der Hilst, R.D., 2008. The geological evolution of
871 the Tibetan Plateau. Science 321, 1054-1058.
872

873 Rudnick, R.L., Gao, S., 2003. In *The Crust* 1-64, Vol. 3 of *Treatise in Geochemistry*
874 (Elsevier, Amsterdam, 2003).
875

876 Sella, G.F, Dixon, T.H., Mao, A., 2002. REVEL: A model for recent plate velocities
877 from space geodesy. Journal of Geophysical Research 107(B4), 2081.
878

879 Sone, M., Metcalfe, I., 2008. Parallel Tethyan sutures in mainland Southeast Asia:
880 New insights for Palaeo-Tethys closure and implications for the Indosinian orogeny.

881 Comptes Rendus Geoscience 340(2), 166-179.

882

883 Sudo, A., Tatsumi, Y., 1990. Phlogopite and K-amphibole in the upper mantle:
884 Implication for magma genesis in subduction zones. Geophysical Research Letters
885 17(1), 29-32.

886

887 Sun, S.S., McDonough, W.F., 1989. Chemical and isotopic systematics of oceanic
888 basalts: implications for mantle composition and processes. Geological Society,
889 London, Special Publications 42, 313-345.

890

891 Sun, C.H., Stern, R.J., 2001. Genesis of Mariana shoshonites: Contribution of the
892 subduction component. Journal of Geophysical Research 106(B1), 589-608.

893

894 Tanaka, T., Togashi, S., Kamioka, H., Amakawa, H., Kagami, H., Hamamoto, T.,
895 Yuhara, M., Orihashi, Y., Yoneda, S., Shimizu, H., Kunimaru, T., Takahashi, K.,
896 Yanagi, T., Nakano, T., Fujimaki, H., Shinjo, R., Asahara, Y., Tanimizu, M.,
897 Dragusanu, C., 2000. JNdi-1: a neodymium isotopic reference in consistency with
898 LaJolla neodymium. Chemical Geology 168, 279-281.

899

900 Tapponnier, P., Zhiqin, X., Roger, F., Meyer, B., Arnaud, N., Wittlinger, G., Jingsui, Y.,
901 2001. Oblique stepwise rise and growth of the Tibet Plateau. Science 294, 1671-1677.

902

903 Thirlwall, M.F., 1991. Long-term reproducibility of multicollector Sr and Nd isotope
904 ratio analysis. *Chemical Geology* 94, 85-104.

905

906 Tunini, L., Jimenez-Munt, I., Fernandez, M., Verges, J., Villasenor, A., Melchiorre, M.,
907 Afonso, J.C., 2016. Geophysical-petrological model of the crust and upper mantle in
908 the India-Eurasia collision zone. *Tectonics* 35(7), 1642-1669.

909

910 Turner, S., Arnaud, N., Liu, J., Rogers, N., Hawkesworth, C., Harris, N., Kelley, S.,
911 van Calsteren, P., Deng, W., 1996. Post-collision, shoshonitic volcanism on the
912 Tibetan Plateau: Implications for convective Thinning of the Lithosphere and the
913 source of ocean island basalts. *Journal of Petrology* 37, 45-71.

914

915 Turner, S., Hawkesworth, C., Liu, J., Rogers, N., Kelley, S., van Clasteren, P., 1993.
916 Timing of Tibetan uplift constrained by analysis of volcanic rocks. *Nature* 364, 50-54.

917

918 Wang, E., Wan, J., Liu, J., 2003. Late Cenozoic geological evolution of the foreland
919 basin bordering the West Kunlun range in Pulu area: Constraints on timing of uplift of
920 northern margin of the Tibetan Plateau. *Journal of Geophysical Research: Solid Earth*
921 108, B8.

922

923 Wang, Q., McDermott, F., Bollon, H., Zhu, Y.T., 2005. Cenozoic K-rich adakitic
924 volcanic rocks in the Hohxil area, northern Tibet: Lower-crustal melting in an

925 intracontinental setting. *Geology* 33(6), 465-468.

926

927 Wang, Q., Hawkesworth, C.J., Wyman, D., Chung, S.L., Wu, F.Y., Li, X.H., Li, Z.X.,

928 Guo, G.N., Zhang, X.Z., Tang, G.J., Dan, W., Ma, L., Dong, Y.H., 2016.

929 Pliocene-Quaternary crustal melting in central and northern Tibet and insights into

930 crustal flow. *Nature Communications* 7, 11888.

931

932 Wang, Z., 2004. Tectonic evolution of the western Kunlun orogenic belt, western

933 China. *Journal of Asian Earth Sciences* 24, 153-161.

934

935 Wei, W., Xu, J., Yu, H., Wei, F., 2015. Origin of the Ashi volcano, Western Kunlun

936 Mountains: Evidence from seismic tomography. *Earth Science Frontiers* 6, 227-232

937 (In Chinese with English Abstract).

938

939 Wei, W., Zhao, D., Xu, J., Zhou, B., Shi, Y., 2016. Depth variation of P-wave

940 azimuthal anisotropy beneath Mainland China. *Scientific Reports* 6: 29614.

941

942 Weis, D., Frey, F.A., 1991. Isotope geochemistry of the Ninetyeast Ridge basement

943 basalts: Sr, Nd, and Pb evidence for involvement of the Kerguelen hot spot. *Proc.*

944 *Ocean Drill Program Sci. Results* 121, 591-610.

945

946 Weis, D., Frey, F.A., 1996. Role of the Kerguelan Plume in generating the eastern

947 India Ocean seafloor. *Journal of Geophysics Research: Solid Earth* 101(B6),
948 13831-13849.

949

950 Weyer, S., Munker, C., Mezger, K., 2003. Na/Ta, Zr/Hf and REE in the depleted
951 mantle: implications for the differentiation history of the crust-mantle system. *Earth
952 and Planetary Science Letter* 205, 309-324.

953

954 White, W.M., 2015. Probing the earth's deep interior through geochemistry.
955 *Geochemical Perspectives* 4(2), 95-250.

956

957 Whittington A.G., Hofmeister A.M., Nabelek, P.I., 2009. Temperature-dependent
958 thermal diffusivity of the Earth's crust and implications for magmatism. *Nature* 458,
959 319-321.

960

961 Williams, H.M., Turner, S.P., Pearce, J.A., Kelley, S.P., Harris, N.B.W., 2004. *Nature*
962 of the source regions for post-collisional, potassic magmatism in southern and
963 northern Tibet from Geochemical variations and inverse trace element modelling.
964 *Journal of Petrology* 45(3), 555-607.

965

966 Wittlinger, G., Tapponnier, P., Poupinet, G., Mei, J., Danian S., Herquel, G., Masson,
967 F., 1998. Tomographic evidence for localized lithospheric shear along the Altyn Tagh
968 fault. *Science* 282, 74-76.

969

970 Wittlinger, G., Vergne, J., Tapponnier, P., Farra, V., Poupinet, G., Jing, M., Su, H.,
971 Herquel, G., Paul, A., 2004. Teleseismic imaging of subducting lithosphere and Moho
972 offsets beneath western Tibet. *Earth and Planetary Science Letters* 221, 117-130.

973

974 Wyllie, P.J., Sekine, T., 1982. The formation of mantle phlogopite in subduction zone
975 hybridization. *Contributions to Mineralogy and Petrology* 79(4), 375-380.

976

977 Xia, L., Li, X., Ma, Z., Xu, X., Xia, Z., 2011. Cenozoic volcanism and tectonic
978 evolution of the Tibetan plateau. *Gondwana Research* 19, 850-866.

979

980 Xu, J., Zhao, B., Zhang, L., Chen, Z., 2012. Field geological exploration of the
981 Ashikule Volcano Group in Western Kunlun Mountains. *Earthquake Research in*
982 *China* 26(2), 152-159.

983

984 Xu, J., Zhao, B., Sindney, H., Chen, Z.Q., Zhang, L.Y., 2014. Geological features and
985 eruption history of Ashikule volcano clusters in western Kunlun Mountain. *Acta*
986 *Petrological Sinica*, 30(12), 3521-3530 (in Chinese with English Abstract).

987

988 Xu, X., Tan, X., Yu, G., Wu, G., Fang, W., Chen, J., Song, H., Shen, J., 2013. Normal-
989 and oblique-slip of the 2008 Yutian earthquake: Evidence for eastward block motion,
990 northern Tibetan Plateau. *Tectonophysics* 584, 152-165.

991

992 Yang, J.H., Chung, S.L., Zhai, M.G., Zhou, X.H., 2004. Geochemical and Sr-Nd-Pb
993 isotopic compositions of mafic dikes from Jiaodong Peninsula, China: evidence for
994 vein-plus-peridotite melting in the lithospheric mantle. *Lithos* 73, 145-160.

995

996 Yu, H., Xu, J., Zhao, B., Shen, H., Lin, C., 2014. Magmatic processes of Ashi Volcano,
997 western Kunlun Mountains, China. *Acta Geologica Sinica (English Edition)* 88(2),
998 530-543.

999

1000 Zhang, P.Z., Shen, Z., Wang, M., Gan, W., Burgmann, R., Molnar, P., Wang, Q., Niu,
1001 Z., Sun, J., Wu, J., Hanrong, S., Xinzhao, Y., 2004. Continuous deformation of the
1002 Tibetan Plateau from global positioning system data. *Geology* 32(9), 809-812.

1003

1004 Zhao, J., Yuan, X., Liu, H., Kumar, P., Pei, S., Kind, R., Zhang, Z., Teng, J., Ding, L.,
1005 Gao, X., Xu, Q., Wang, W., 2010. The boundary between the Indian and Asian
1006 tectonic plates below Tibet. *Proceedings of the National Academy of Sciences*,
1007 107(25), 11229-11233.

1008

1009 Zhisheng, A., Kutzbach, J.E., Prell, W.L., Porter, S.C., 2001. Evolution of Asian
1010 monsoons and phased uplift of the Himalaya-Tibetan plateau since Late Miocene
1011 times. *Nature* 411, 62-66.

1012

Zindler, A., Hart, S., 1986. Chemical geodynamics. *Annual Review of Earth and Planetary Sciences* 14, 493-571.

Figure Captions

Fig. 1. (a) Tectonic map of the northwest margin of the Tibetan Plateau, modified after Furuya and Yasuda (2011), Xu et al. (2013) and Bie and Ryder (2014). Black, green and red focal mechanisms represent the main shocks of the 2008, 2012 and 2014 earthquakes, respectively, according to the Global Centroid-Moment-Tensor (CMT) catalog. (b) Geological map of the Ashikule volcanic basin (AVB), modified after Liu and Maimaiti (1989) and Xu et al. (2012). Red arrows represent the direction of the lava flow. Black open circles represent the location of lava samples, and the ID of samples is also marked with a black arrow. Locations of main volcanoes in the AVB are marked with red triangles. AS: Ashi Volcano; DH: Dahei Volcano; XS: Xishan Volcano; MT: Mati Volcano; DS: Dong volcano; HL: Heilong Volcano; MN: Maoniu Volcano; YY: Yueya Volcano; MG: Migong Volcano; WL: Wuluke Volcano; YZ: Yizi Volcano; GT: Gaotai Volcano; BH: Binhu Volcano; YS: Yin Volcano.

Fig. 2. Vertical cross sections of P-wave anisotropy tomography (isotropic velocities only are shown) along 3 profiles shown on the inset map (see Wei et al., 2016 for details of the method). (a) Vertical cross section of 80°E suggests that the Indian slab has collided with the Tarim slab. (b) Vertical cross section of 81.53°E (on the AVB) suggests that there is a small gap between the two slab beneath the AVB. (c) Vertical cross section of 83°E displays a wider gap between the two slabs.

Fig. 3. Photomicrographs of four representative volcanic rocks in the AVB under cross-polarised light. Cpx, clinopyroxene; Opx, orthopyroxene; Phl, phlogopite; Pl, plagioclase. (a) Sample ASKL-5. Phenocrysts of orthopyroxene and plagioclase showing disequilibrium textures including extensive embayments. (b) Sample 513-11. Phenocrysts of clinopyroxene, plagioclase and phlogopite in a highly vesicular matrix. (c) Sample ASKL-12. A large plagioclase glomerocryst in a crystalline matrix. (d) Sample 518-9. Phenocrysts of clinopyroxene, plagioclase and orthopyroxene in a porphyritic texture.

Fig. 4. Classification for lava samples in the AVB: (a) SiO_2 versus $\text{Na}_2\text{O} + \text{K}_2\text{O}$ (wt%), (b) Na_2O versus K_2O (wt%). The boundaries of diagram (a) and (b) are from Le Bas et al. (1986) and Miller et al. (1999), respectively.

Fig. 5. Major element variation diagrams for the studied samples in AVB. Symbols are as in Fig. 2. The most recent lava sample (ASKL-3) is marked with a cross inside the circle.

Fig. 6. Primitive mantle-normalized trace element (a) and chondrite-normalized rare earth element patterns (b) for AVB lavas. Primitive mantle and chondrite normalization values are from Sun and McDonough (1989). EMII (Samoa) (Jackson et al., 2007), globally subducting sediment (GLOSS; Plank and Langmuir, 1998) and upper continental crust (UCC, Rudnick and Gao, 2003) compositions are presented for comparison.

Fig. 7. (a) Primitive mantle-normalized La/Yb ratios $((\text{La}/\text{Yb})_n)$ versus MgO (wt%); (b) $((\text{La}/\text{Yb})_n)$ versus La (ppm). (c) Eu anomaly (Eu/Eu^*) versus MgO (wt%); Eu/Eu^*

1057 $= Eu_n \times 2 / (Sm_n + Gd_n)$; Eu_n , Sm_n and Gd_n are the primitive mantle-normalized Eu,
1058 Sm and Gd concentrations of studied sample, respectively. (d) Ti anomaly (Ti/Ti^*)
1059 versus SiO_2 (wt%); $Ti/Ti^* = Ti_n \times 2 / (Eu_n + Tb_n)$; Ti_n and Tb_n are the primitive mantle
1060 –normalized Ti and Tb, respectively. (e) Ba/Th ratios versus Th/Nd ratios. (f) Th/La
1061 ratios versus Sm/La ratios. Symbols are as in Fig. 2.

1062 Fig. 8. Present day $^{87}Sr/^{86}Sr$ versus $^{143}Nd/^{144}Nd$ for lavas from the AVB. Literature
1063 data specifically from the AVB are presented for comparison (Cooper et al., 2002;
1064 Guo et al., 2006, 2014; Williams et al., 2004). Enriched mantles (EM I, EM II), bulk
1065 silicate earth (BSE), Indian and Pacific MORB fields are modified from Zindler and
1066 Hard (1986) and White (2015).

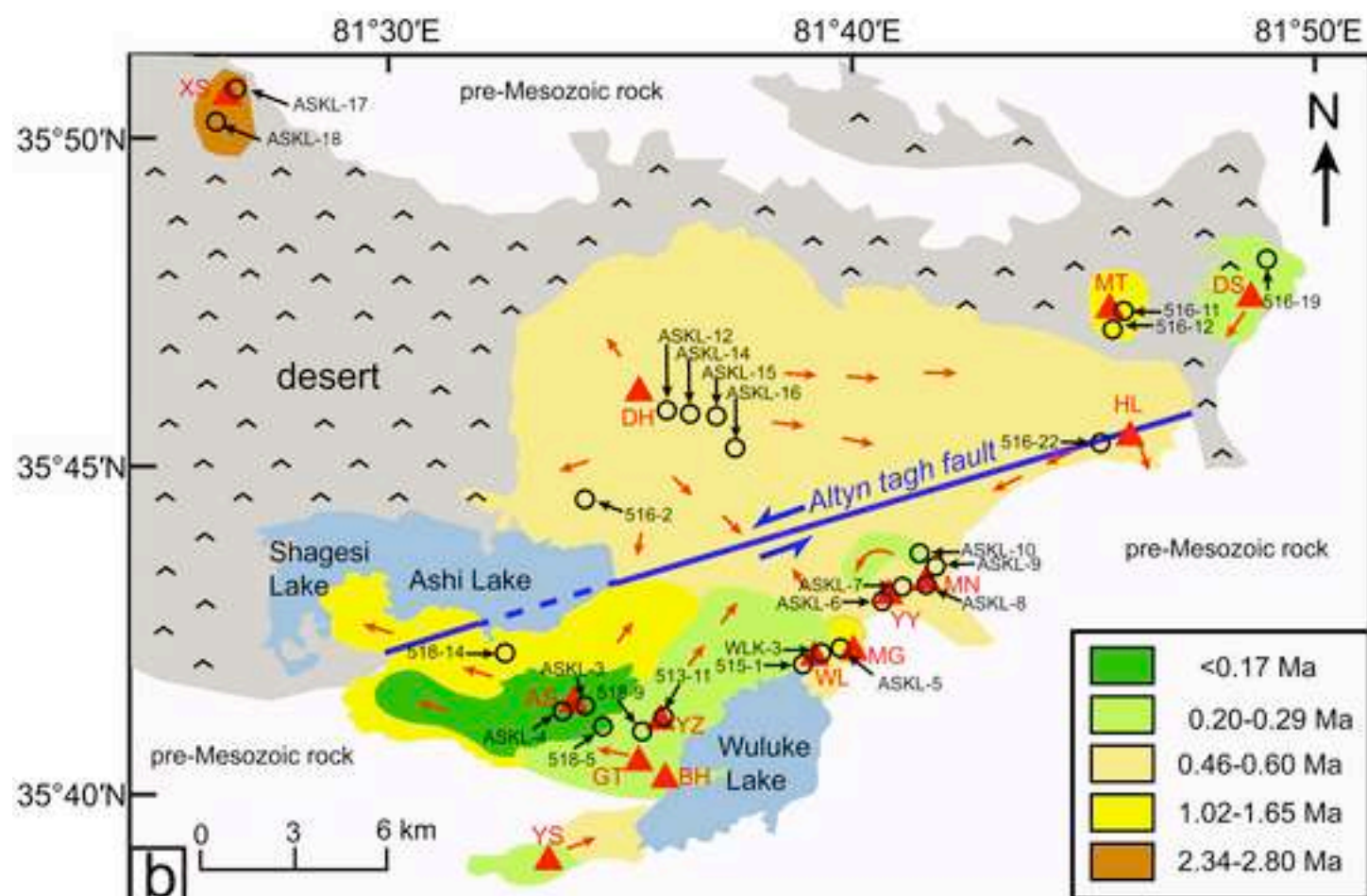
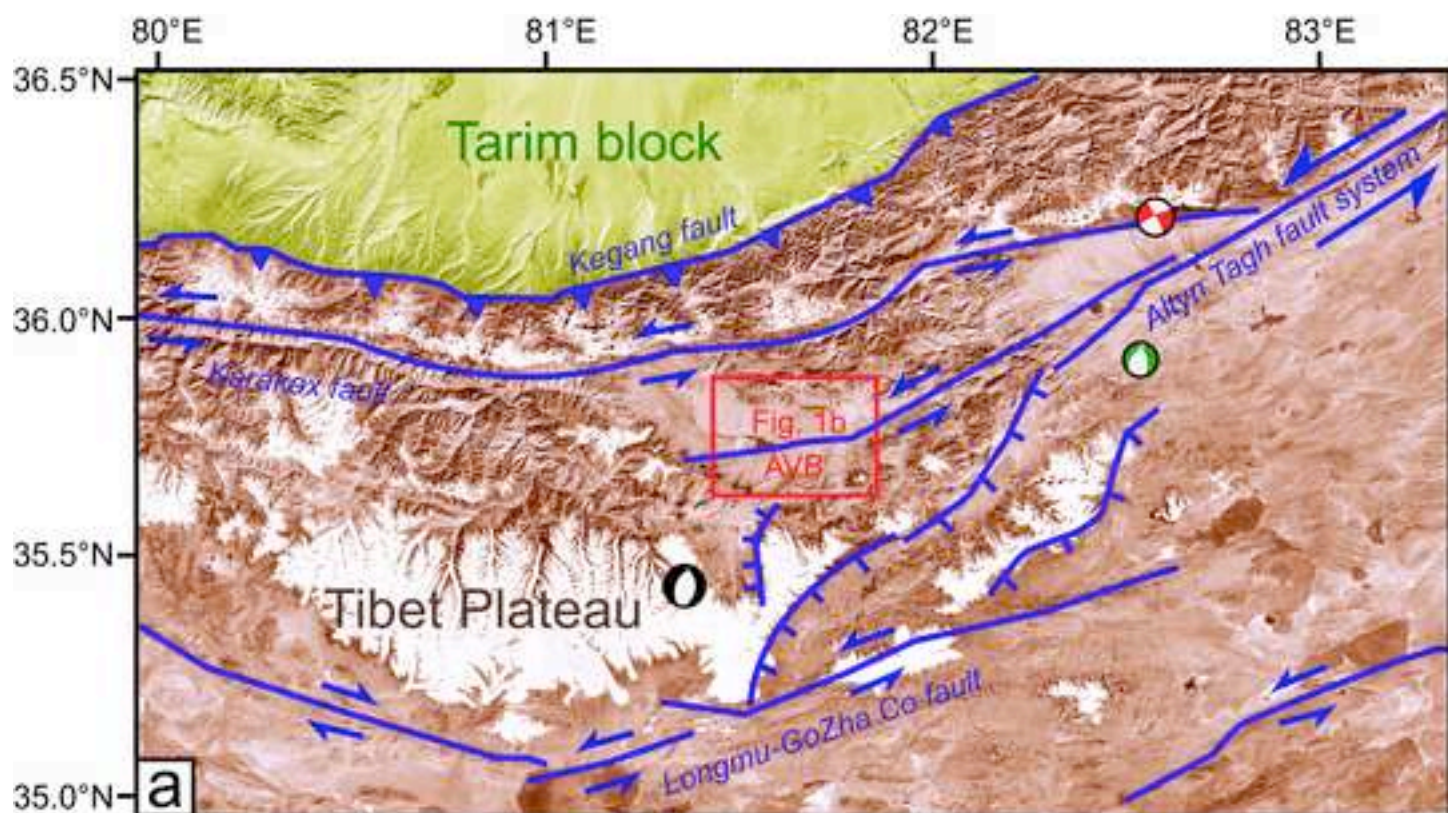
1067 Fig. 9. SiO_2 versus $^{87}Sr/^{86}Sr$ (a) and $^{143}Nd/^{144}Nd$ ratios (b) for the AVB lavas. Symbols
1068 as in Figure 2.

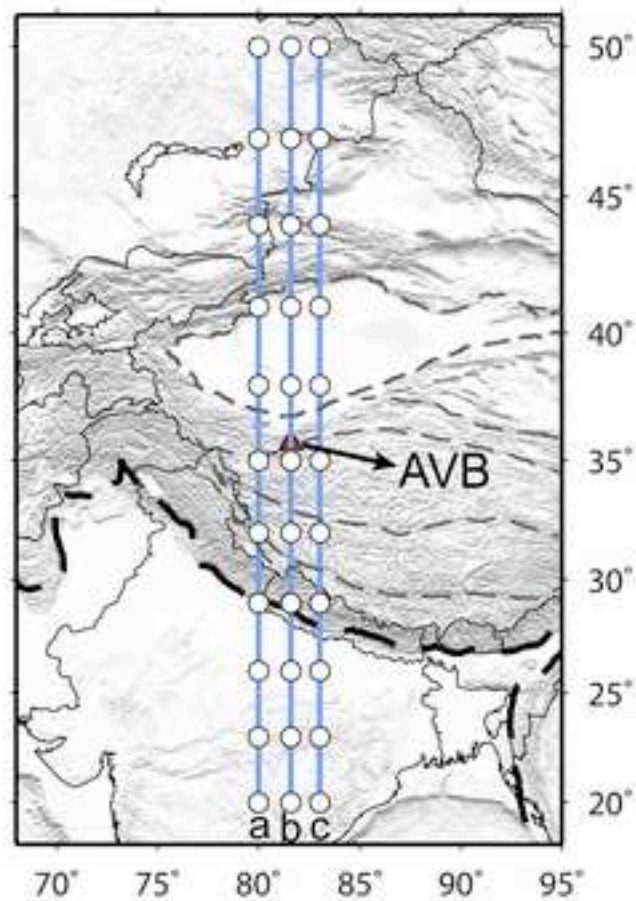
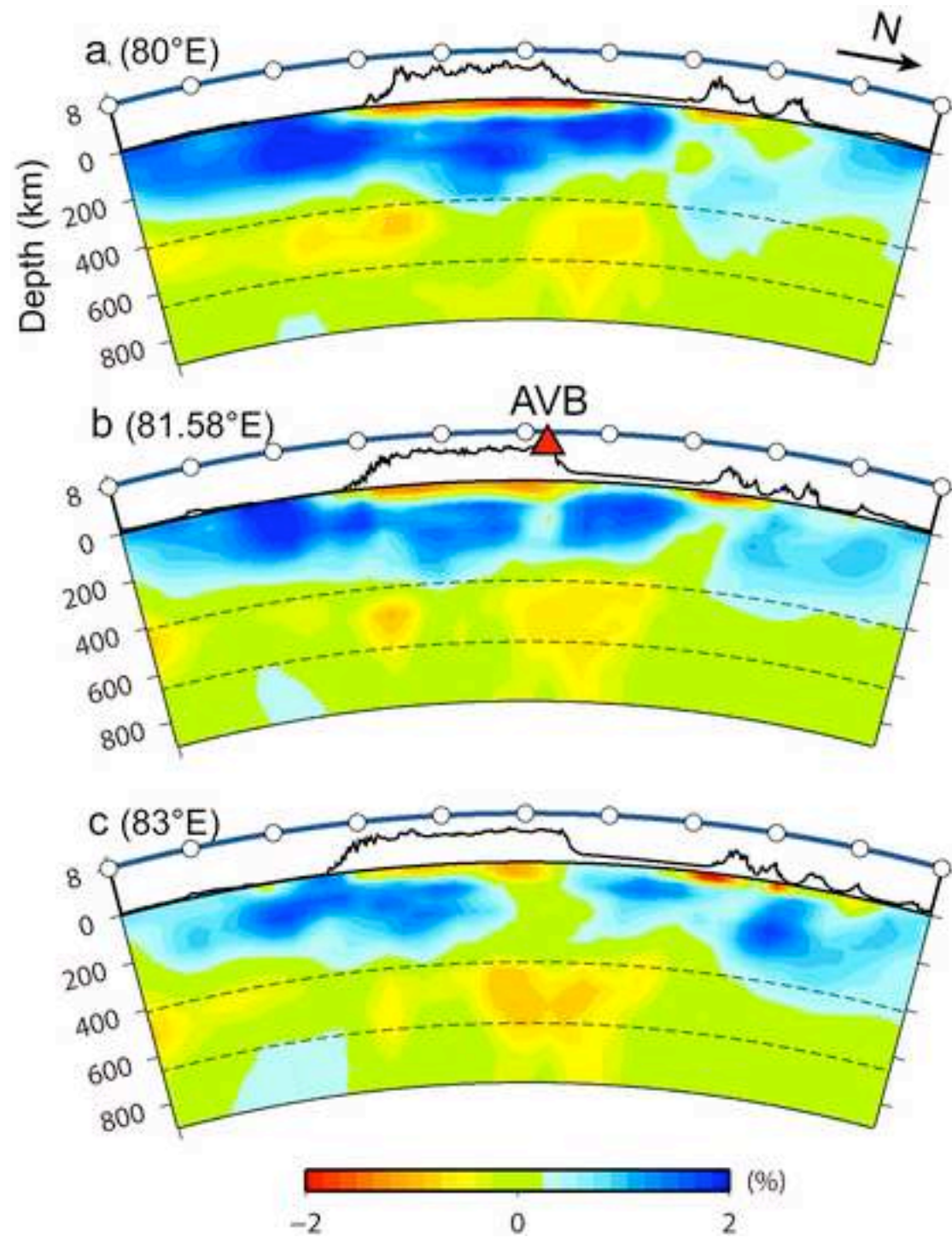
1069 Fig. 10. Zr/Hf versus Nb/Ta ratios of the AVB lavas. Plots of upper continental crust
1070 (UCC; Rudnick and Gao, 2003), primitive mantle (PM; Sun and McDonough, 1989),
1071 global subducting sediments (GLOSS; Plank and Langmuir, 1998) and EM II Samoan
1072 source (Jackson et al., 2007) are displayed for comparison.

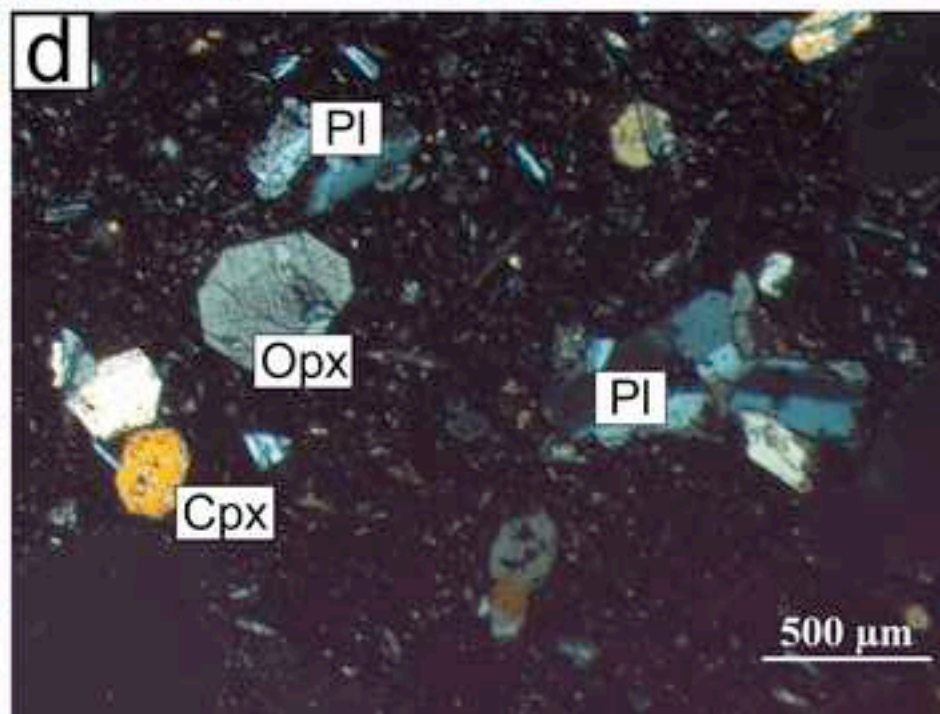
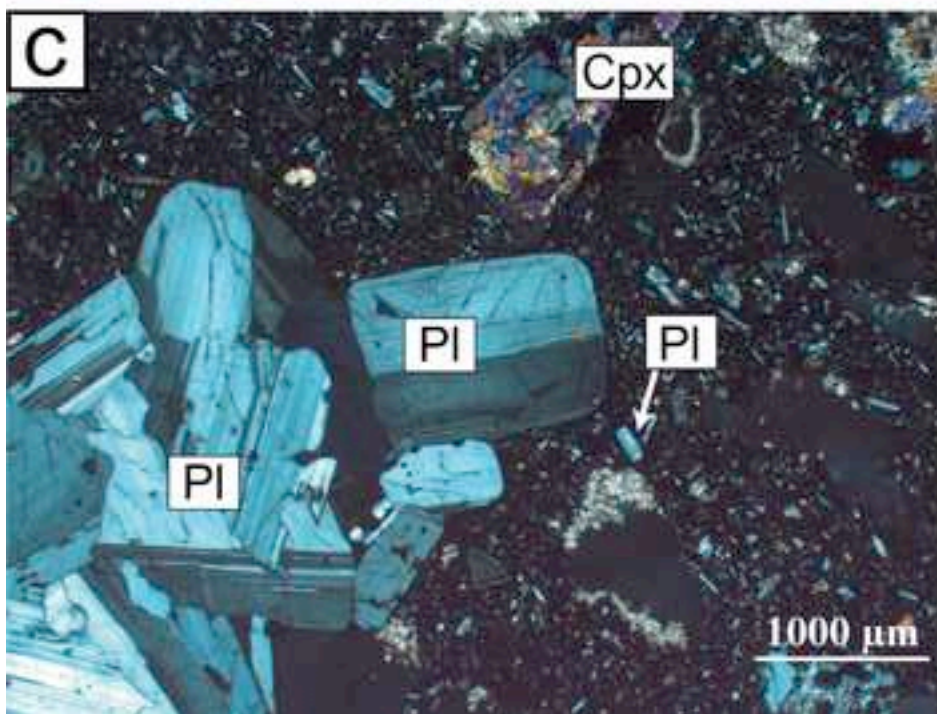
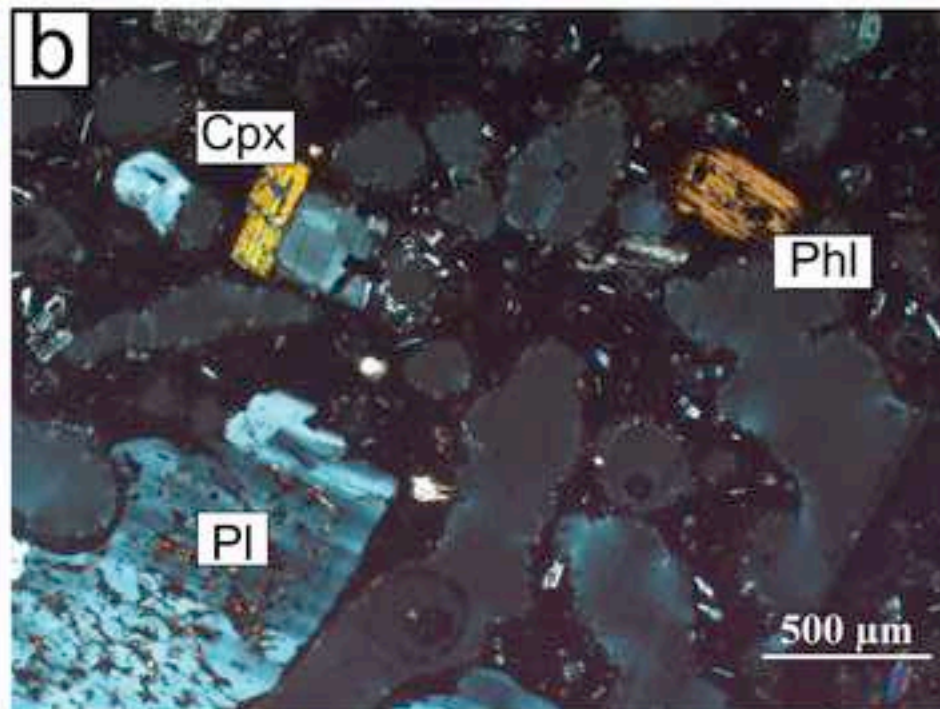
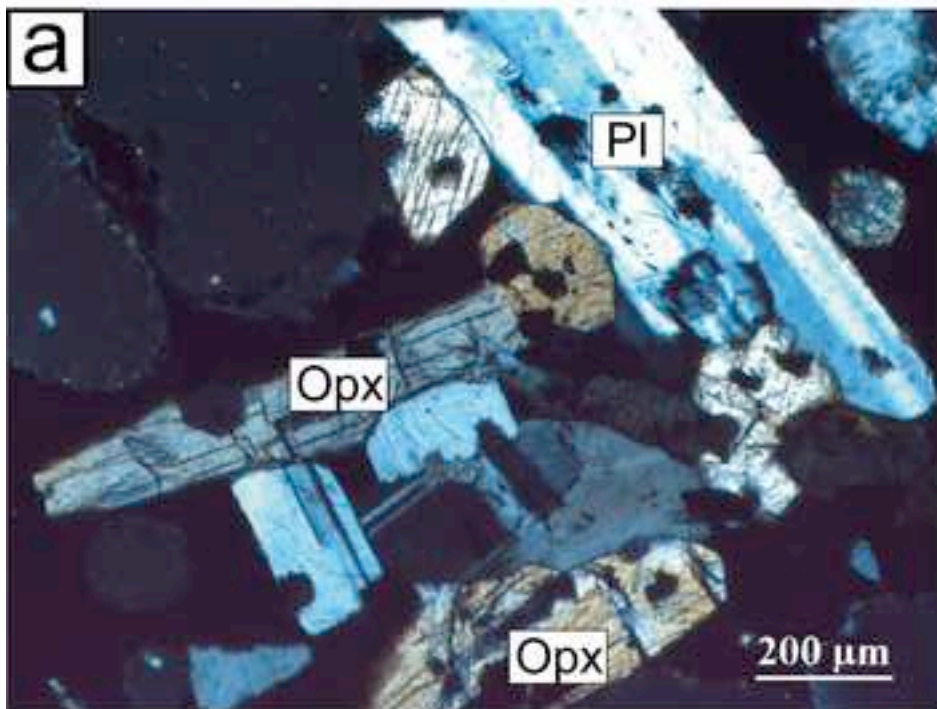
1073 Fig. 11. Rb/Sr versus Ba/Rb for the AVB lavas (after Furman and Graham, 1999). The
1074 field of common lithospheric mantle (CLM) is taken from Furman and Graham
1075 (1999).

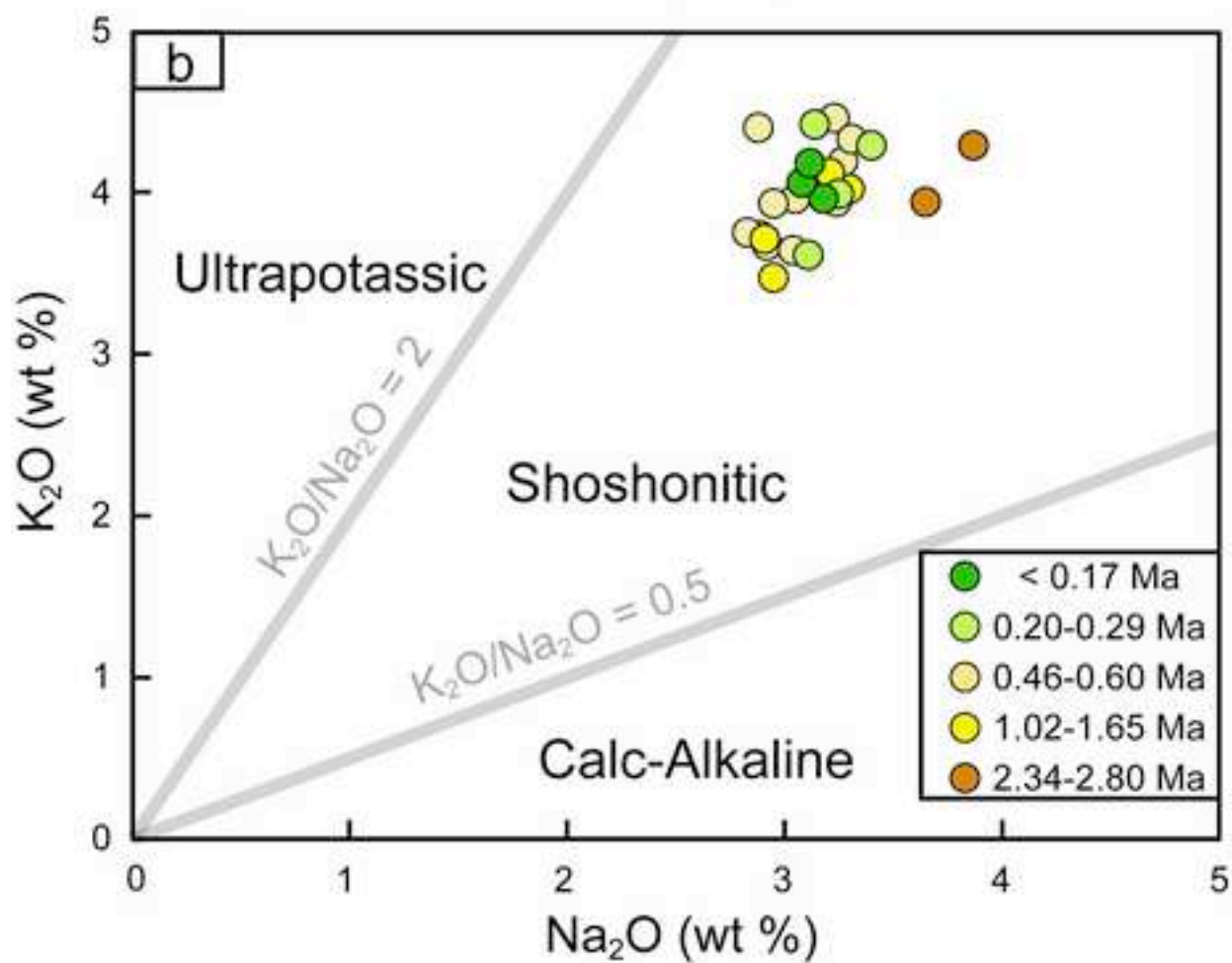
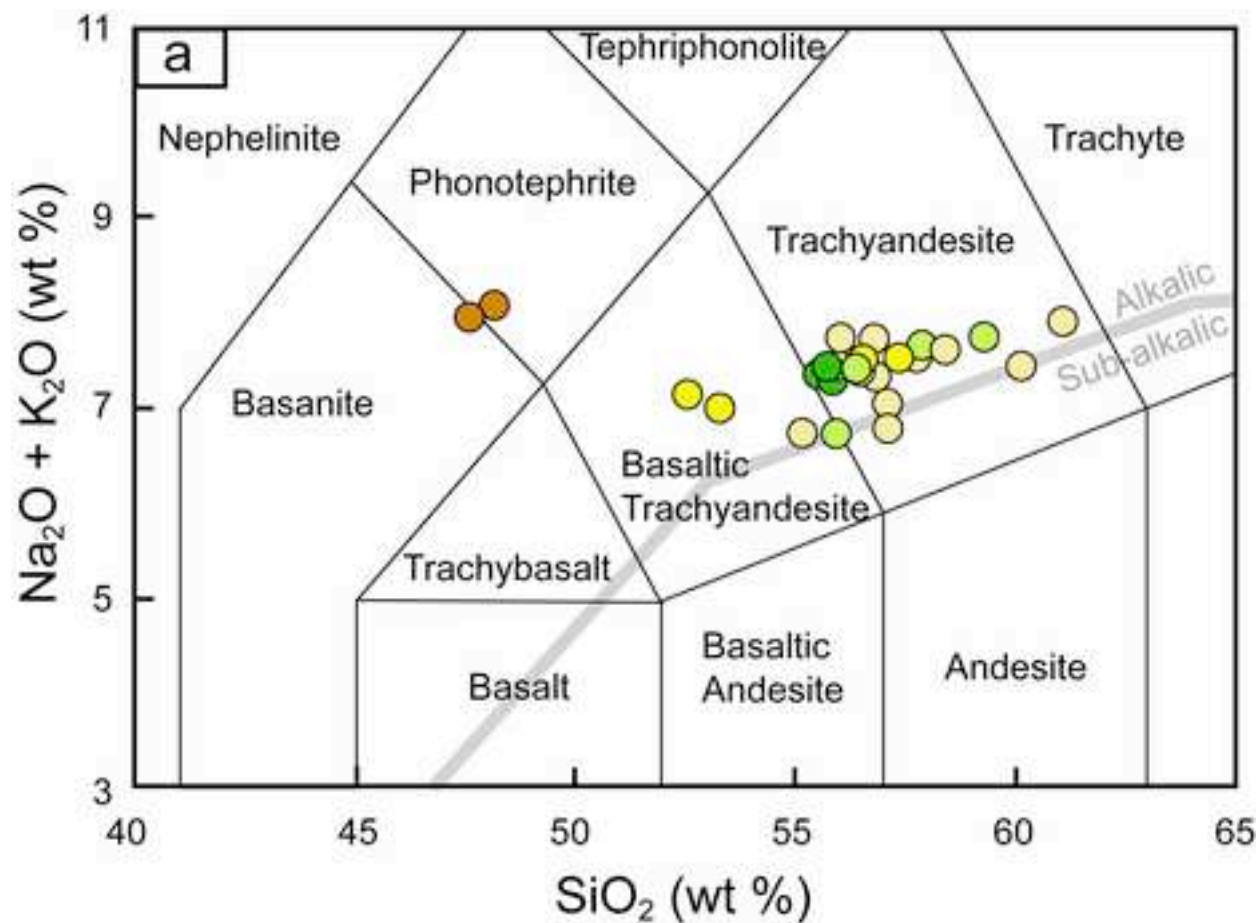
1076 Fig. 12. Schematic model for the post-collisional magmatism in northwestern Tibet
1077 and lithospheric sections of the present settings. The locations and average ages of the
1078 volcanic fields are modified from Guo et al. (2014). In the section of $79^\circ E$, Indian and

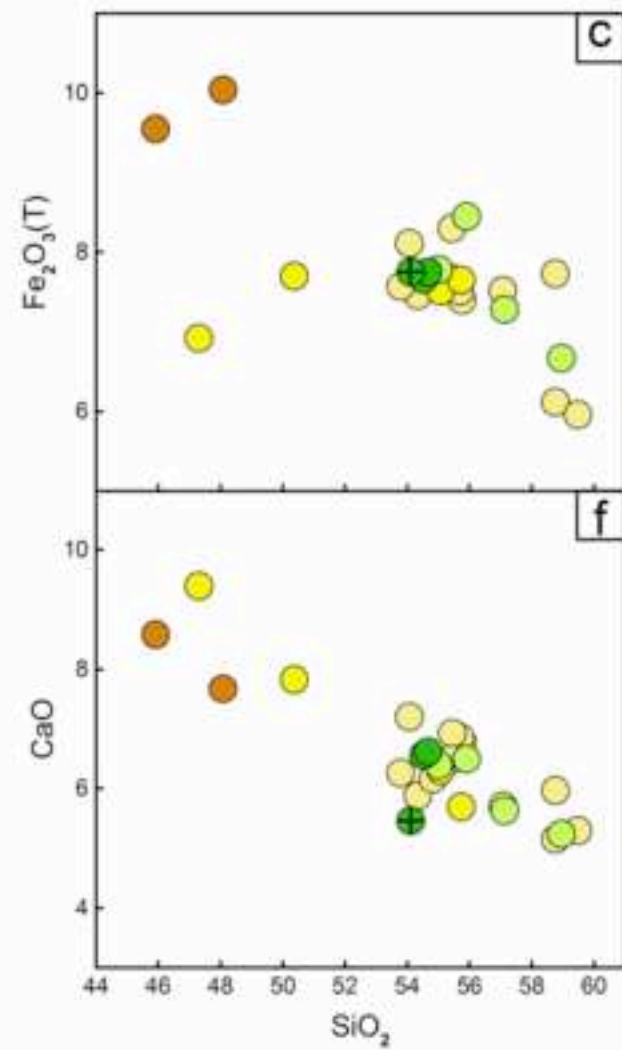
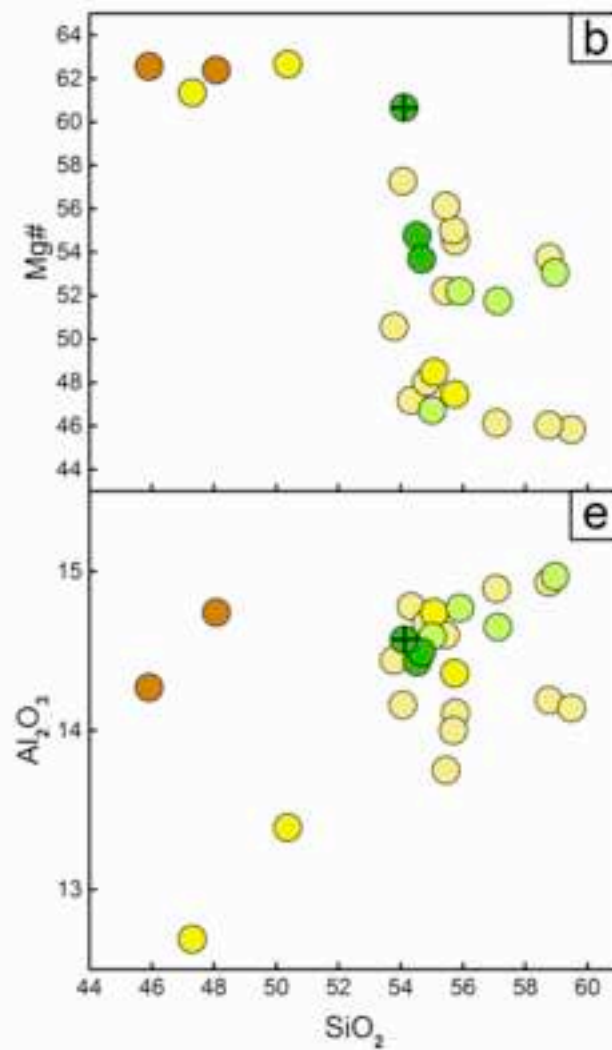
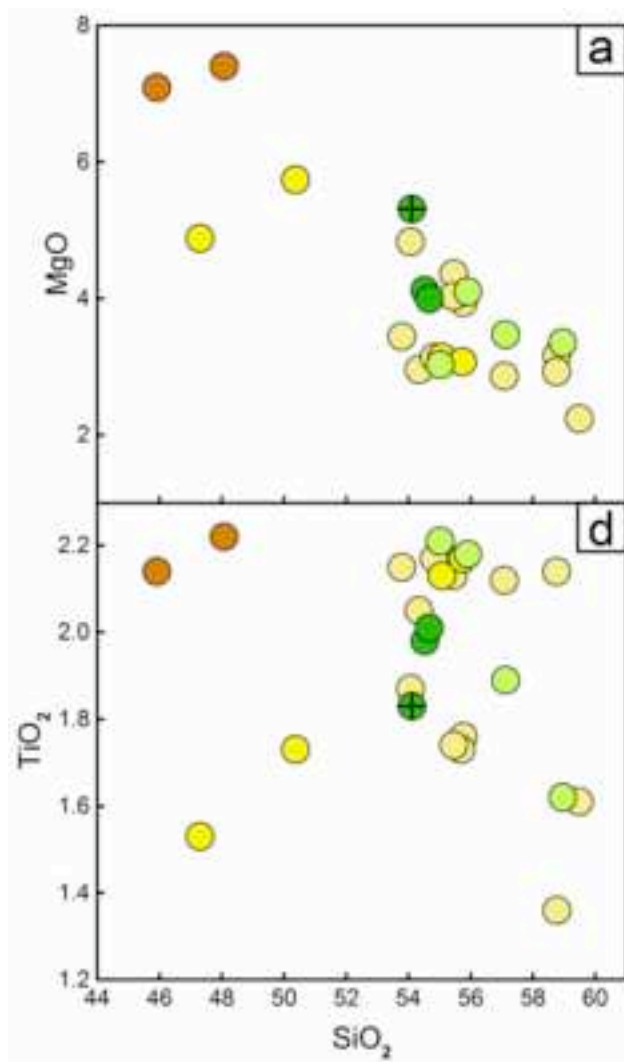
1079 Tarim lithospheres have collided together beneath the west Kunlun Mountains. In the
1080 section of 81°E, the two slabs just collide together. In the section of 83°E, there is a
1081 gap between the Indian and Tarim lithospheres. The progressive closure of this gap
1082 may lead to shear heating, melting of the Tibetan SCLM and focussing of magmatism
1083 with transport along deep-seated lithospheric faults.

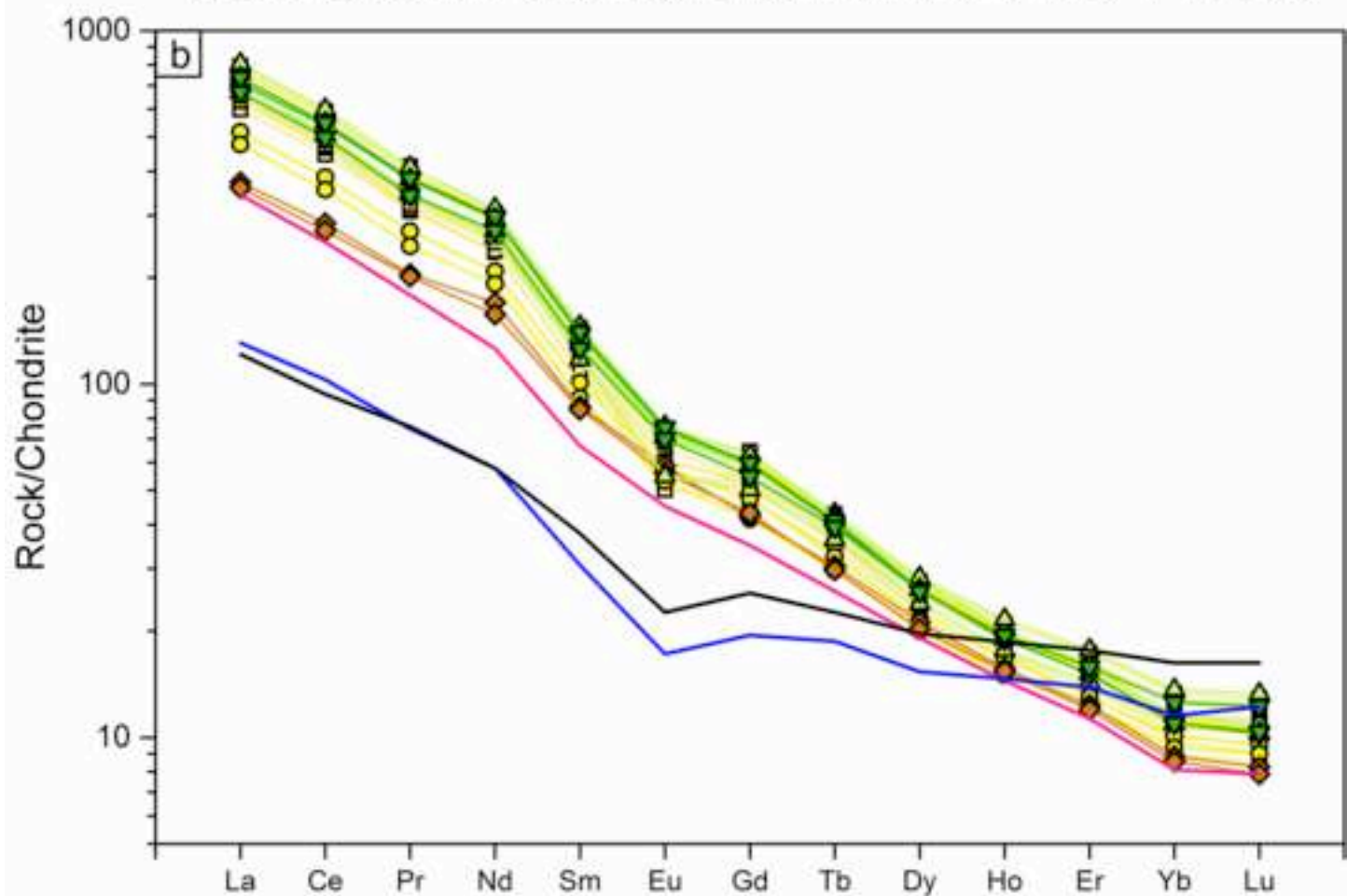
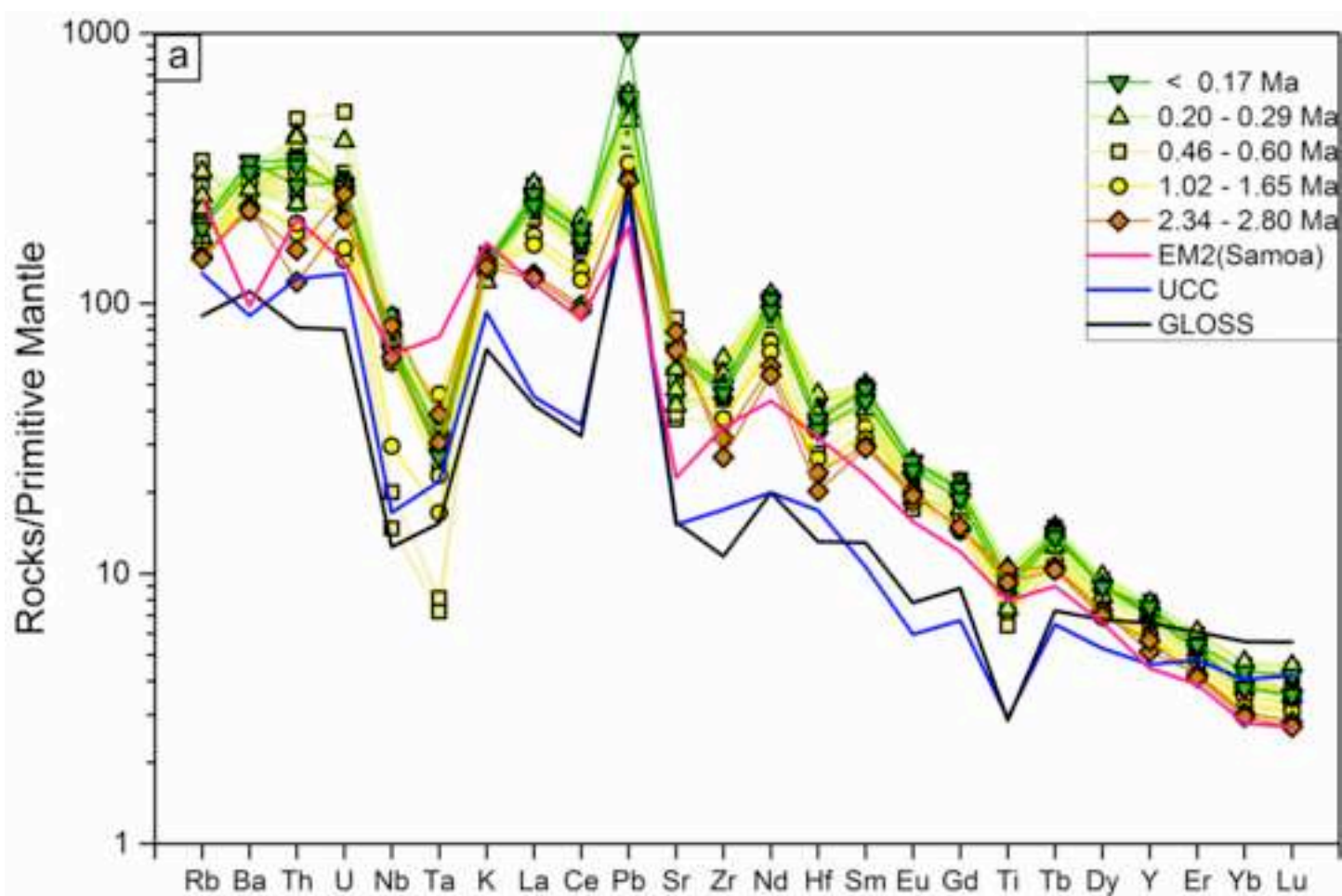


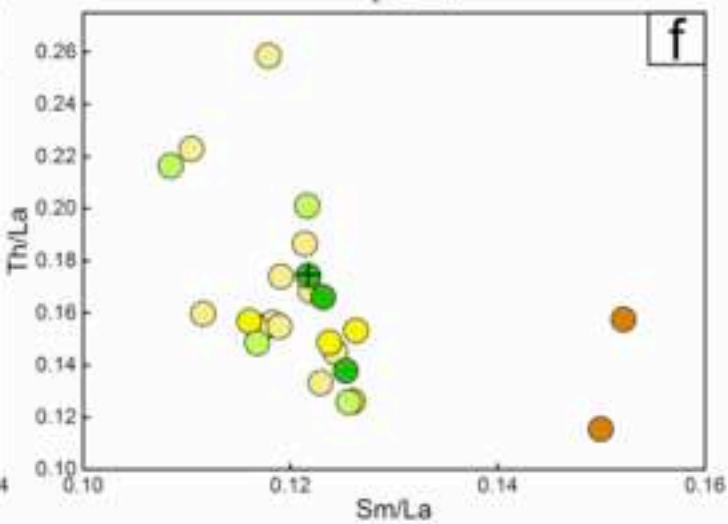
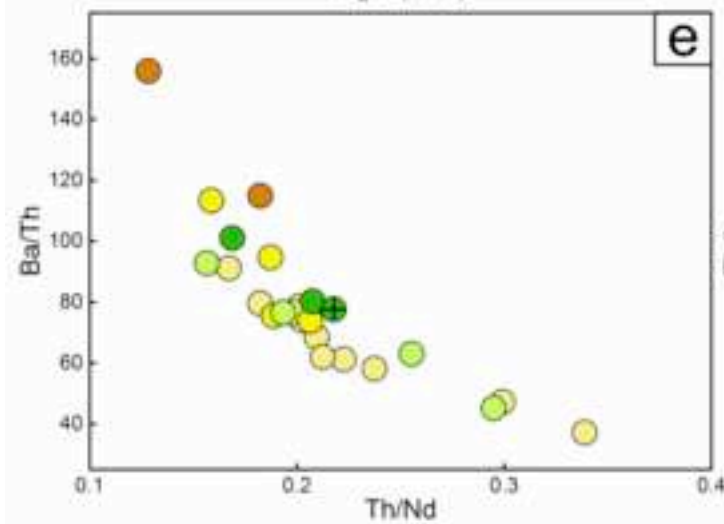
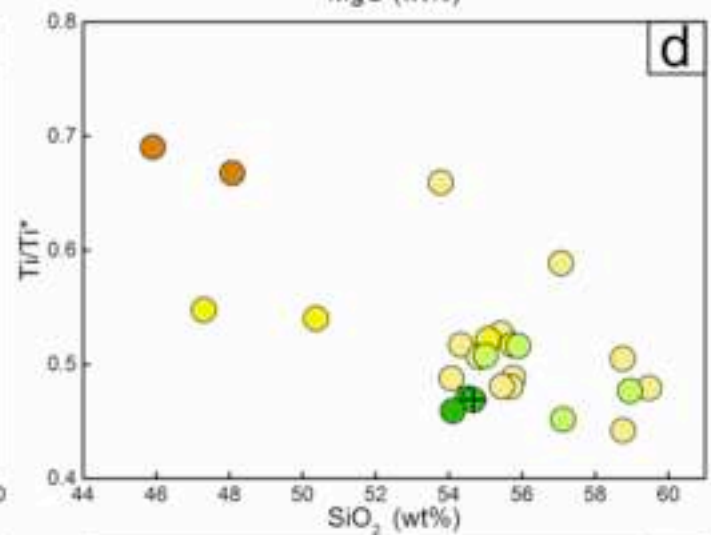
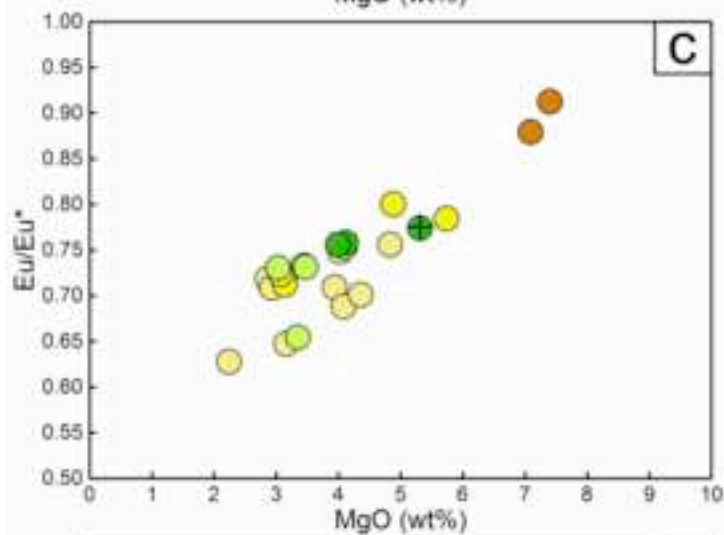
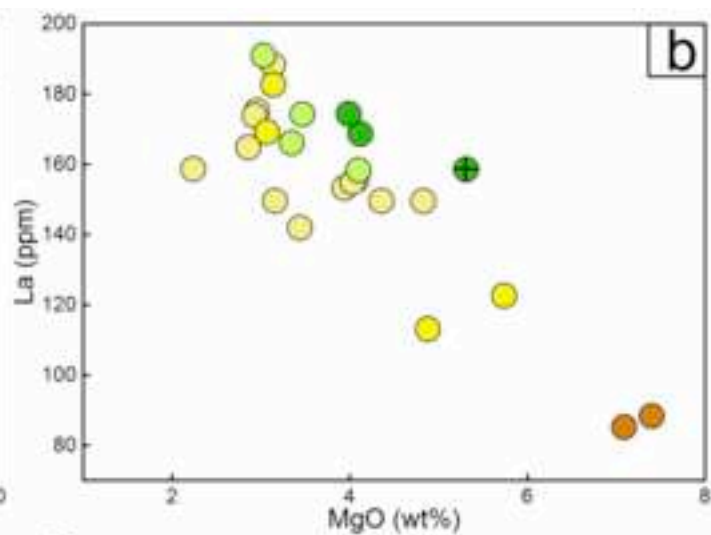
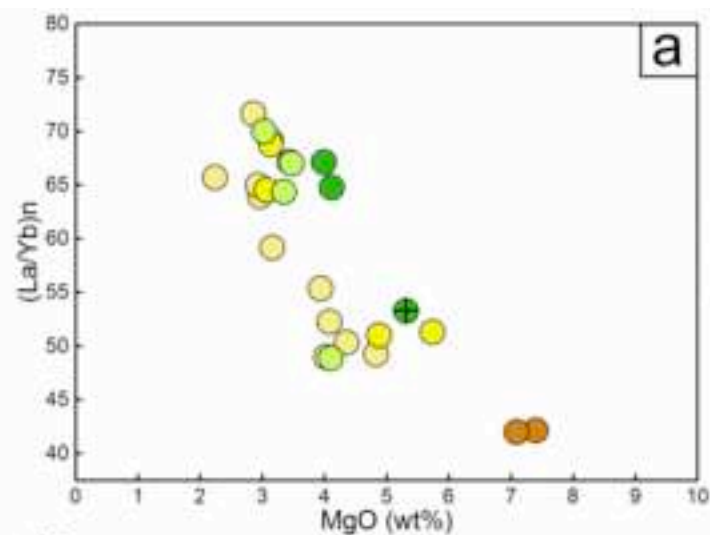


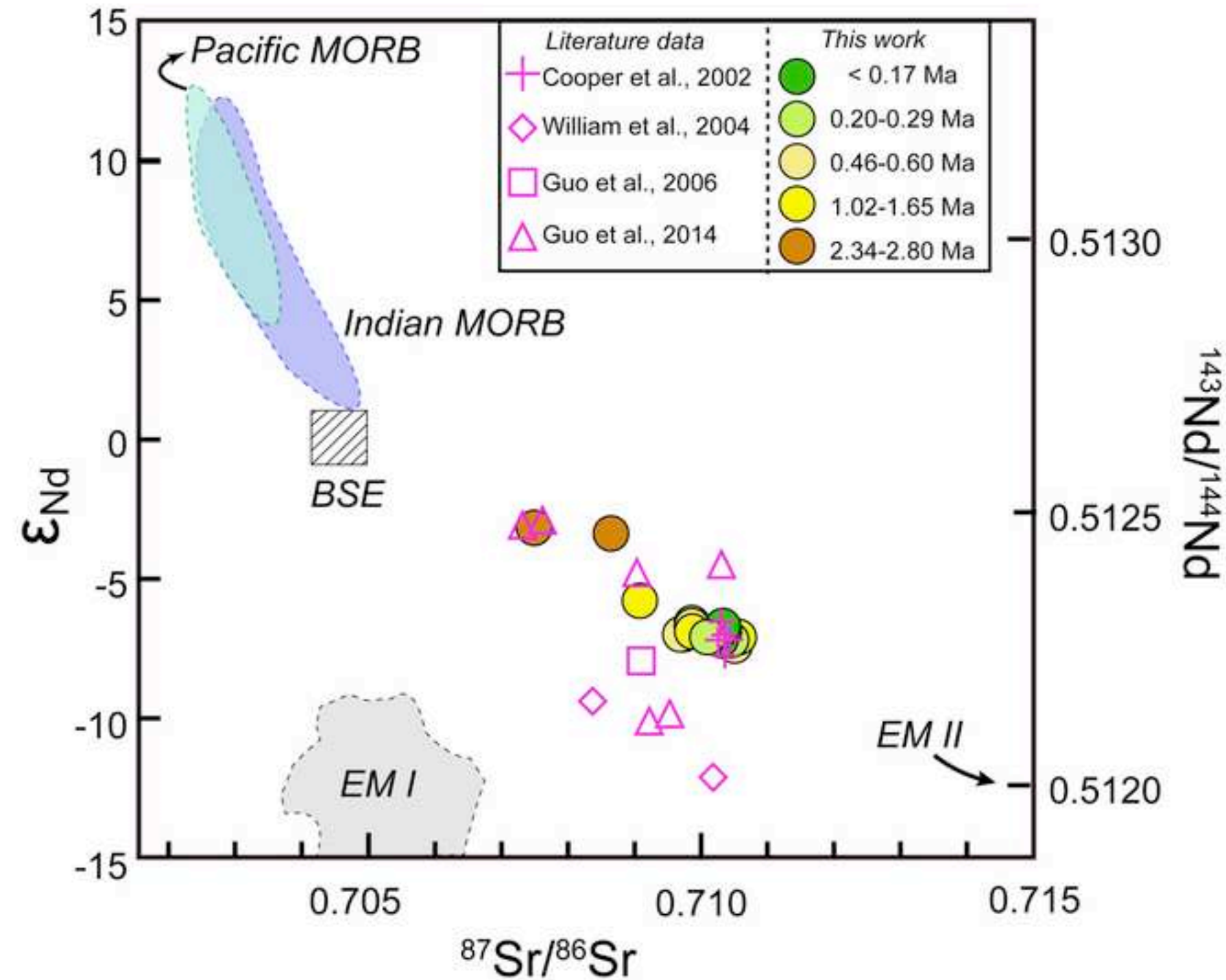


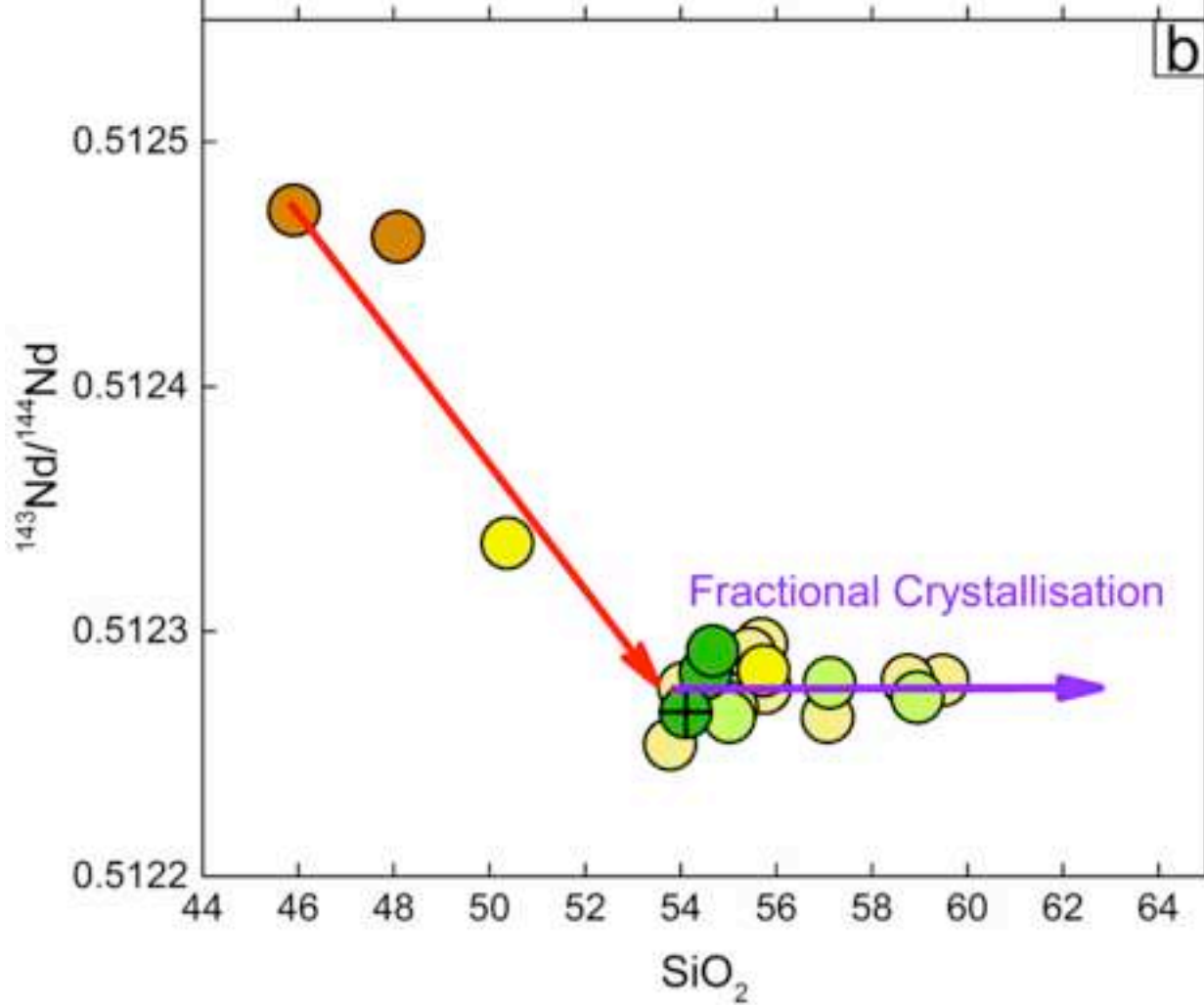
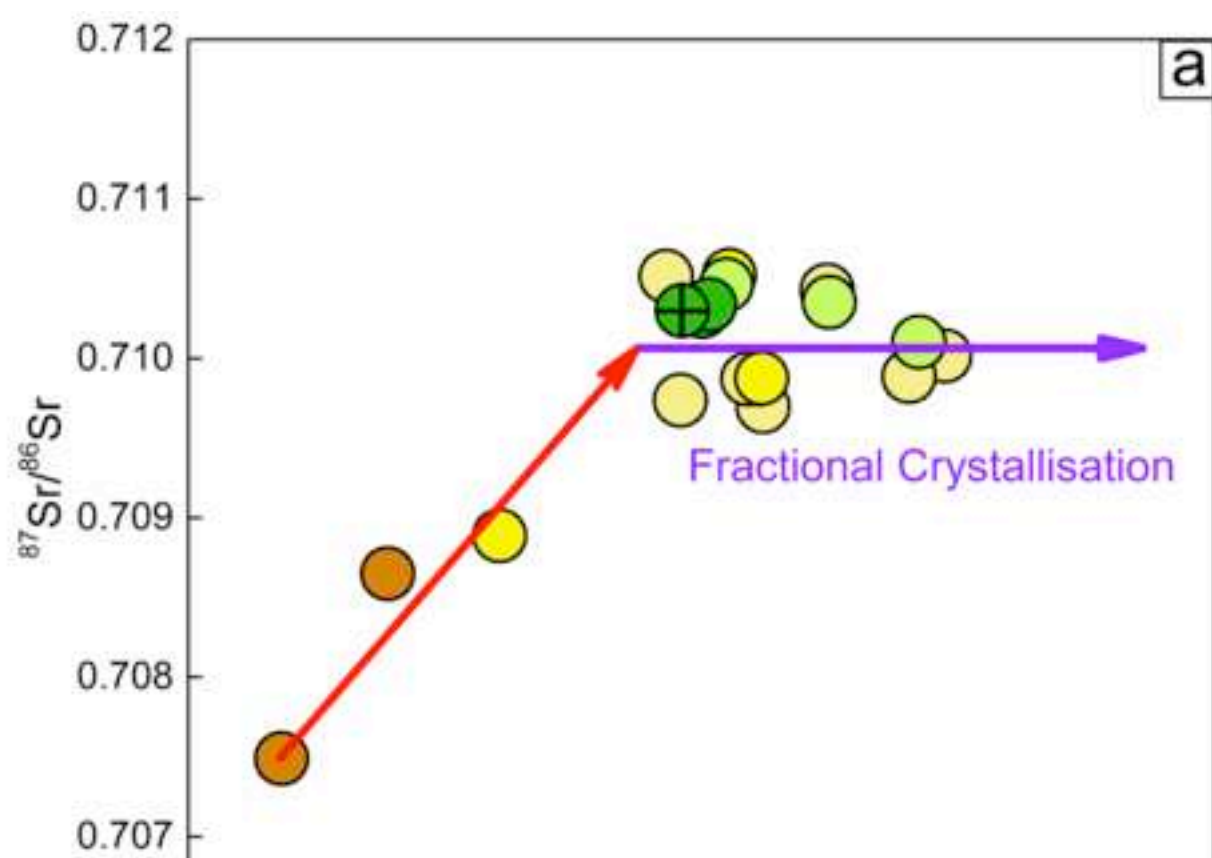


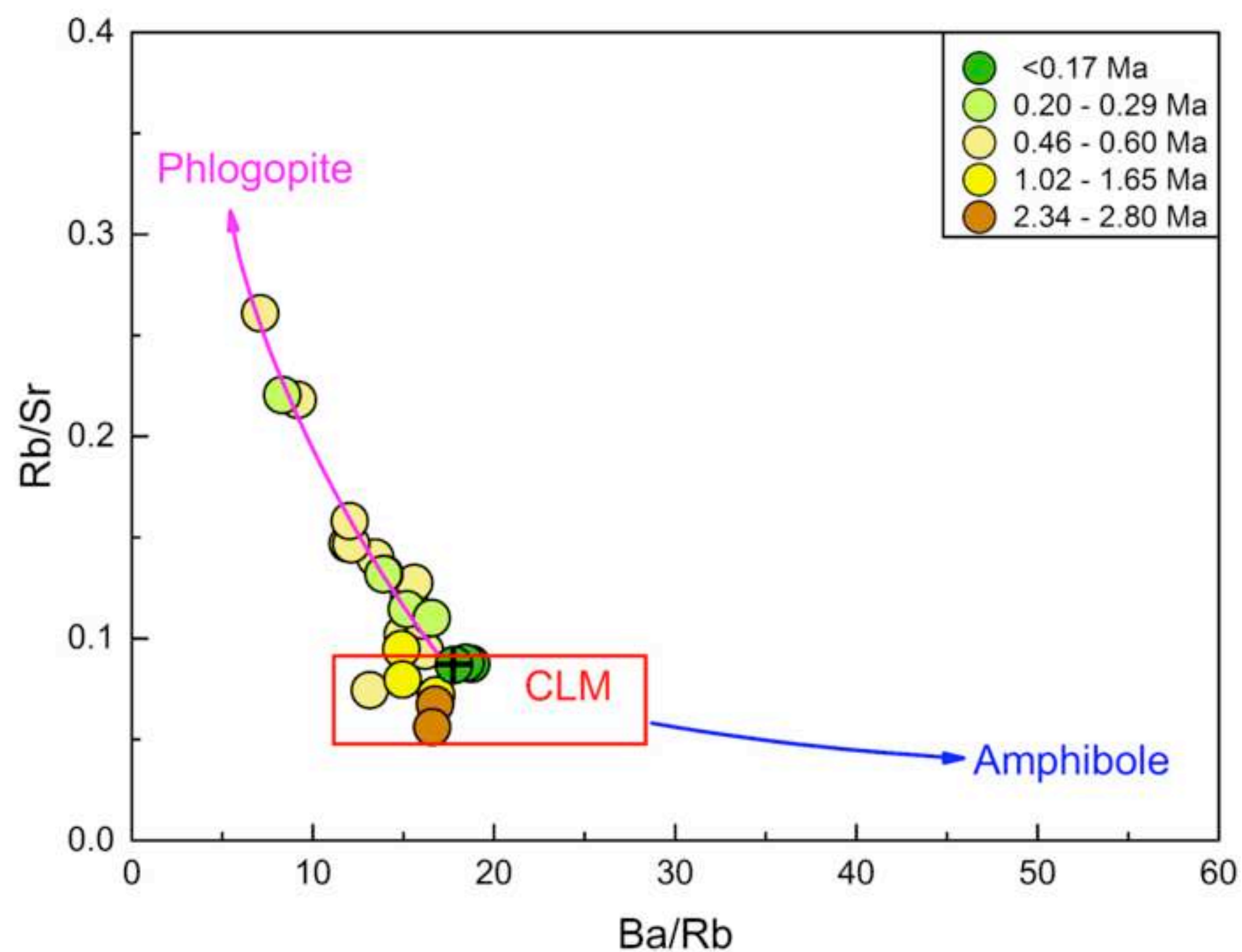












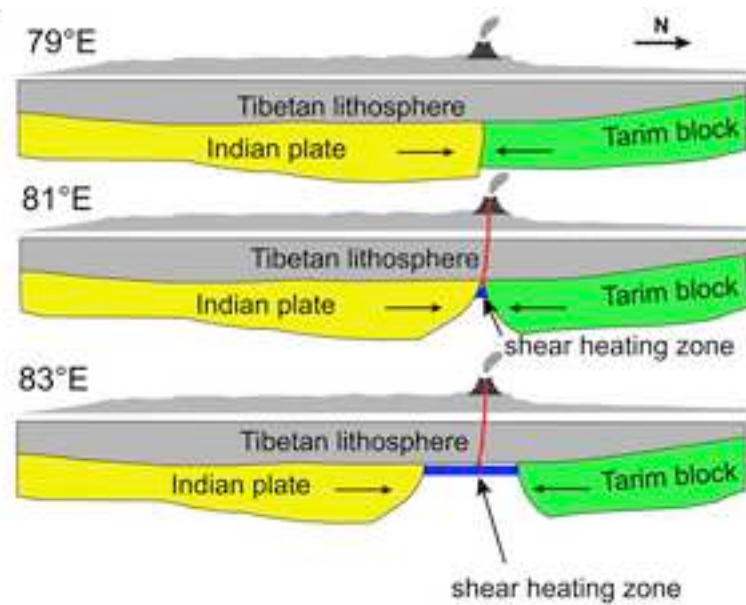
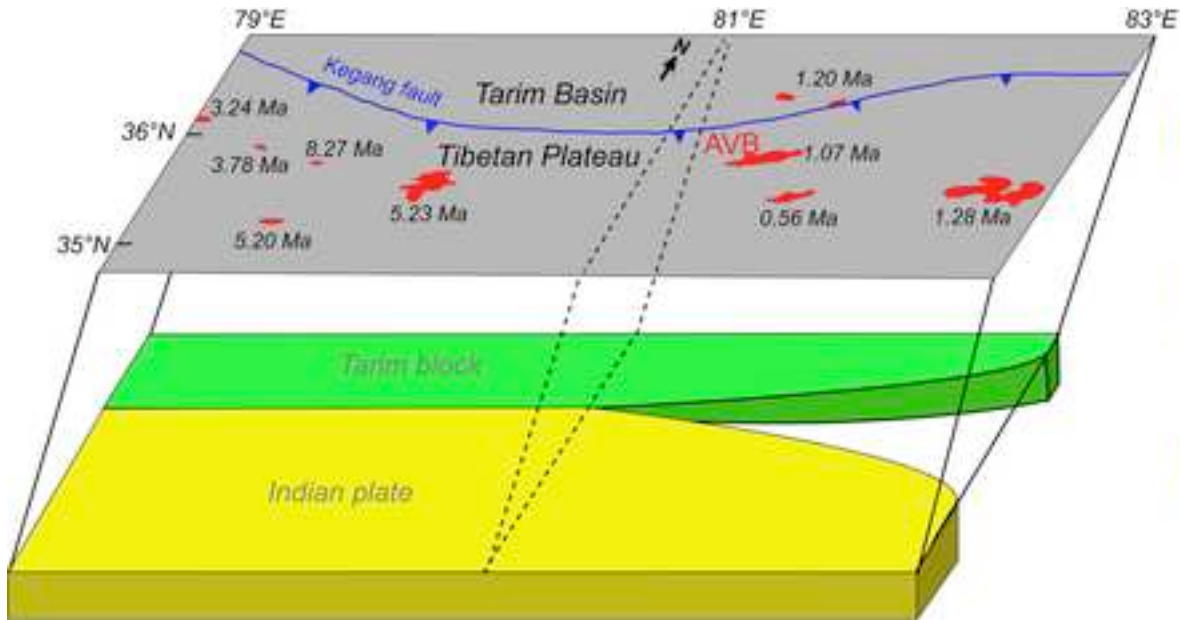


Table 1

Percentage abundance of vesicles, groundmass and phenocrysts in Ashikule volcanic rocks.

Episode (age)	Sample	Vesicle	Groundmass	Phenocrysts	Groundmass
1 and 2 (<0.17 Ma)	ASKL-3	60%	28%	Pl(6)+Cpx(3)+Opx(2)+Ol(1)	G
1 and 2 (<0.17 Ma)	ASKL-4	55%	32%	Pl(1)+Cpx(4)+Opx(6)+Ol(1)+Bi(<1)+Fe-Ti(<1)	Pl+Ol+G
1 and 2 (<0.17 Ma)	518-5	35%	51%	Opx(9)+Cpx(4)+Pl(1)	Pl+Cpx+Opx+G
3 (0.20-0.29 Ma)	ASKL-10	30%	60%	Pl(8)+Opx(1)+Fe-Ti(1)	Pl+Opx+Fe-Ti+G
3 (0.20-0.29 Ma)	513-11	45%	40%	Pl(10))+Cpx(2)+Opx(2)+Phl(1)	Pl+Cpx+Opx+G
3 (0.20-0.29 Ma)	516-19	20%	74%	Pl(4)+Opx(1)+Cpx(1)	Pl+Ol+Cpx+Opx+G
3 (0.20-0.29 Ma)	518-9	45%	39%	Pl(10)+Cpx(3)+Opx(2)+ Fe-Ti(1)	Pl+Cpx+Opx+Fe-Ti+G
4 (0.46-0.60 Ma)	ASKL-6	80%	15%	Pl(<1)+Cpx(3) +Opx(<1)+Ol(<1)+Fe-Ti(<1)	Fe-Ti+G
4 (0.46-0.60 Ma)	ASKL-7	20%	65%	Pl(12)+ Opx(2)+Cpx(<1)	G
4 (0.46-0.60 Ma)	ASKL-8	25%	42%	Pl(25)+ Opx(4)+Cpx(2)+ Fe-Ti(2)	Pl+Opx+Fe-Ti+G
4 (0.46-0.60 Ma)	ASKL-9	40%	38%	Pl(16) + Opx(5)+Cpx(1)+ Fe-Ti(<1)	Pl+Opx+Ol+Fe-Ti+G
4 (0.46-0.60 Ma)	ASKL-12	10%	58%	Pl(22)+ Opx(4)+Cpx(3)+Phl(1)+Fe-Ti(2)	Pl+OPX+CPX+Ol+G
4 (0.46-0.60 Ma)	ASKL-14	25%	66%	Pl(5)+Opx(4)	Pl+Opx+G
4 (0.46-0.60 Ma)	ASKL-15	30%	52%	Pl(7)+Cpx(6)+Opx(5)	Pl+Ol+Cpx+Opx+Fe-Ti+G
4 (0.46-0.60 Ma)	ASKL-16	15%	58%	Pl(15)+Opx(8)+Cpx(2)+Phl(1)+Fe-Ti(1)	Pl+Opx+Cpx+G
4 (0.46-0.60 Ma)	515-1	15%	68%	Pl(12)+Opx(2)+Phl(2)+Cpx(1)	Pl+Phl+Cpx+Opx+G
4 (0.46-0.60 Ma)	WLK-3	30%	61%	Pl(6)+Opx(2)+Ol(<1)+Fe-Ti(<1)	Pl+Cpx+Opx+Fe-Ti+G
4 (0.46-0.60 Ma)	516-2	25%	56%	Cpx(11)+Opx(6)+Pl(2)	Pl+Cpx+Opx+G
4 (0.46-0.60 Ma)	516-22	40%	57%	Pl(2)+ Cpx(2)+Opx(1)	Pl+Cpx+G
5 (1.02-1.65 Ma)	ASKL-5	50%	34%	Pl(11)+ Opx(2)+Fe-Ti(2)+Cpx(1)	Pl+Cpx+G
5 (1.02-1.65 Ma)	516-11	40%	48%	Opx(6)+Cpx(3)+Pl(2)+Fe-Ti(1)	Pl+Cpx+Opx+G
5 (1.02-1.65 Ma)	516-12	50%	39%	Opx(6)+ Pl(4)+Cpx(1)	Pl+Cpx+G
5 (1.02-1.65 Ma)	518-14	30%	64%	Pl(2)+Opx(2)+Cpx(1)+Fe-Ti(1)	Pl+Cpx+Opx+Fe-Ti+G
6 (2.34-2.80 Ma)	ASKL-17	30%	57%	Cpx(9)+Opx(4)	Pl+Cpx+Opx+G
6 (2.34-2.80 Ma)	ASKL-18	30%	55%	Cpx(12)+Opx(2)+Pl(1)	Pl+Cpx+Opx+Fe-Ti+G

Pl = plagioclase; Cpx = clinopyroxene; Opx = orthopyroxene; Phl = phlogopite; Fe-Ti = Fe-Ti oxides; G = glass. Numbers in the brackets after the phenocrysts indicate the visually estimated volumetric percentages of the different phenocryst types in the thin section.

Table 2

Whole-rock trace and major element results for volcanic rocks from Ashikule Volcanoes.

Episode (age)	1 and 2 (<0.17 Ma)			3 (0.20-0.29 Ma)				4 (0.46-0.60 Ma)					
Sample	ASKL-3	ASKL-4	518-5	ASKL-10	513-11	516-19	518-9	ASKL-6	ASKL-7	ASKL-8	ASKL-9	ASKL-12	ASKL-14
<i>(wt %)</i>													
SiO ₂	54.11	54.52	54.67	55.01	58.95	55.9	57.12	54.33	53.78	57.07	54.82	58.76	54.07
TiO ₂	1.83	1.98	2.01	2.21	1.62	2.18	1.89	2.05	2.15	2.12	2.17	1.36	1.87
Al ₂ O ₃	14.57	14.43	14.49	14.59	14.97	14.77	14.65	14.78	14.44	14.89	14.67	14.19	14.16
Fe ₂ O ₃ (T)	7.75	7.66	7.75	7.78	6.67	8.45	7.28	7.46	7.57	7.52	7.65	6.12	8.11
MnO	0.11	0.11	0.11	0.11	0.09	0.12	0.1	0.10	0.11	0.10	0.11	0.09	0.12
MgO	5.31	4.12	3.99	3.03	3.35	4.10	3.47	2.96	3.44	2.86	3.14	3.16	4.83
CaO	5.46	6.56	6.62	6.39	5.24	6.50	5.63	5.88	6.26	5.71	6.16	5.97	7.20
Na ₂ O	3.18	3.08	3.12	3.25	3.4	3.11	3.14	3.05	3.19	3.27	3.24	2.88	2.92
K ₂ O	3.97	4.07	4.19	4.00	4.30	3.62	4.43	3.97	3.98	4.20	3.95	4.41	3.68
P ₂ O ₅	0.99	1.10	1.14	1.23	0.75	1.15	1.01	1.10	1.19	1.15	1.19	0.69	1.01
LOI	2.91	1.48	0.96	1.45	1.27	0.60	1.01	3.70	2.86	1.03	2.68	2.99	1.20
Total	100.19	99.11	99.05	99.05	100.61	100.5	99.93	99.38	98.97	99.92	99.78	100.6	99.2
Mg#	61	55	54	47	53	52	52	47	51	46	48	54	57
<i>(ppm)</i>													
Li	41.2	33.4	29.0	33.6	61.6	26.2	37.9	31.7	30.8	27.1	23.7	34.5	26.5
Sc	14.5	6.31	9.74	10.9	11.0	8.97	11.2	11.0	8.06	8.92	10.7	10.7	9.42
V	105	108	107	98.8	92.2	113	97.9	98.9	74.0	78.7	98.5	78.4	115
Cr	78.5	66.1	66.2	24.6	49.2	71.5	52.9	26.3	14.8	19.0	22.9	75.3	104
Co	20.0	19.7	19.3	16.6	17.5	20.6	17.5	16.4	12.0	12.5	16.9	13.5	22.9
Ni	49.3	43.9	45.8	13.7	41.2	43.7	35.0	13.7	10.4	9.94	14.6	24.0	58.5
Cu	19.8	20.8	20.0	18.8	26.4	25.3	20.9	10.2	17.7	13.7	16.9	14.3	26.5
Zn	131	126	127	143	118	144	133	139	105	114	146	112	125
Rb	120	125	126	143	195	111	159	136	112	134	143	171	112
Sr	1386	1433	1432	1247	885	1012	1203	1130	874	956	1400	786	1193
Y	34.4	31.8	32.6	35.2	32.1	35.5	32.9	33.2	26.6	29.6	33.8	30.8	33.2
Zr	520	555	549	703	521	613	561	562	530	602	610	411	521
Nb	47.0	51.3	50.0	63.4	53.5	57.8	51.9	10.5	47.1	52.9	14.3	46.2	49.0
Cs	3.22	3.27	2.92	2.55	9.42	1.90	4.24	3.80	2.25	2.76	2.69	5.07	2.35
Ba	2144	2348	2322	2169	1620	1846	2205	2074	1740	1800	2136	1570	1814
La	159	169	174	191	166	158	174	175	142	165	188	150	150
Ce	305	329	336	367	311	310	335	334	273	315	362	285	289
Pr	32.5	35.9	36.4	39.0	32.8	33.0	36.0	36.5	29.4	33.2	39.2	29.8	30.7
Nd	127	138	140	147	122	127	137	132	110	126	143	111	119
Sm	19.3	21.1	21.5	22.3	18.0	19.9	21.2	20.7	16.8	18.4	22.0	16.5	18.4
Eu	4.05	4.33	4.38	4.41	3.18	4.11	4.18	4.08	3.33	3.57	4.35	2.91	3.80
Gd	11.3	12.2	12.3	12.9	10.4	12.0	12.1	12.4	9.7	10.6	13.3	9.7	11.0
Tb	1.47	1.51	1.54	1.61	1.36	1.57	1.54	1.50	1.24	1.33	1.60	1.27	1.46
Dy	6.58	6.60	6.69	7.10	6.07	7.21	6.66	6.67	5.38	5.87	6.91	5.81	6.64
Ho	1.10	1.07	1.08	1.14	1.00	1.22	1.08	1.12	0.87	0.95	1.14	0.96	1.13
Er	2.62	2.51	2.50	2.65	2.37	2.93	2.51	2.57	2.04	2.19	2.58	2.31	2.71
Yb	2.14	1.87	1.86	1.96	1.85	2.32	1.87	1.97	1.52	1.65	1.96	1.81	2.18
Lu	0.31	0.26	0.26	0.28	0.26	0.34	0.26	0.28	0.22	0.23	0.27	0.26	0.32
Hf	10.5	11.5	11.5	14.3	10.7	12.6	12.1	10.8	10.7	11.8	12.0	8.64	10.8
Ta	1.11	1.32	1.14	1.59	1.38	1.57	1.23	0.30	1.04	1.15	0.33	1.08	1.56
Tl	8.26	0.66	0.73	0.81	0.15	0.64	0.95	0.29	0.15	1.96	0.62	1.29	0.83
Pb	66.3	39.6	41.2	41.1	36.2	33.7	42.7	39.0	31.4	28.3	42.1	42.2	33.3
Th	27.6	23.2	29.0	28.3	35.9	19.9	35.0	27.2	22.2	26.3	28.9	33.3	19.9
U	5.67	5.87	5.47	5.59	8.39	4.51	5.76	4.88	4.67	5.11	5.65	6.41	5.14

Table 2 (continued)

Episode (age)	4 (0.46-0.60 Ma)						5 (1.02-1.65 Ma)				6 (2.34-2.80 Ma)	
Sample	ASKL-15	ASKL-16	515-1	WLK-3	516-2	516-22	ASKL-5	516-11	516-12	518-14	ASKL-17	ASKL-18
(wt %)												
SiO ₂	55.76	55.69	59.48	58.75	55.45	55.43	55.07	50.37	47.3	55.73	48.08	45.91
TiO ₂	1.76	1.73	1.61	2.14	1.74	2.13	2.13	1.73	1.53	2.17	2.22	2.14
Al ₂ O ₃	14.11	14.00	14.14	14.93	13.75	14.6	14.74	13.39	12.69	14.36	14.74	14.27
Fe ₂ O ₃ (T)	7.40	7.51	5.96	7.73	7.67	8.30	7.51	7.70	6.92	7.65	10.04	9.55
MnO	0.11	0.11	0.08	0.11	0.11	0.12	0.10	0.10	0.09	0.10	0.14	0.13
MgO	3.94	4.08	2.24	2.93	4.36	4.03	3.14	5.74	4.88	3.07	7.40	7.09
CaO	6.78	6.85	5.30	5.15	6.93	6.49	6.30	7.83	9.39	5.69	7.67	8.58
Na ₂ O	2.95	2.89	3.23	3.31	2.83	3.04	3.30	2.91	2.95	3.21	3.87	3.65
K ₂ O	3.94	3.74	4.47	4.34	3.76	3.65	4.03	3.72	3.48	4.13	4.30	3.95
P ₂ O ₅	0.91	0.88	0.83	1.16	0.89	1.12	1.16	0.89	0.77	1.19	1.12	1.07
LOI	1.54	1.49	1.95	0.26	1.38	0.57	1.5	3.21	5.93	1.64	0.41	3.52
Total	99.20	98.97	99.29	100.81	98.87	99.48	98.98	97.59	95.93	98.94	99.99	99.86
Mg#	55	55	46	46	56	52	48	63	61	47	62	63
(ppm)												
Li	29.7	33.6	65.3	45.6	33.1	29.3	30.1	21.1	26.0	35.5	18.6	15.6
Sc	8.80	11.1	8.37	10.4	13.6	13.0	10.0	12.8	11.7	9.83	5.04	13.4
V	101	104	69.2	92.5	109	110	94.5	104	82.7	95.0	146	141
Cr	73.7	88.9	23.8	32.5	95.6	71.2	19.9	142	127	37.2	141	132
Co	20.6	19.2	11.8	16.3	20.2	20.1	15.3	26.5	23.7	16.2	36.9	35.6
Ni	57.7	38.4	11.5	22.8	51.5	46.4	10.4	122	118	21.2	122	107
Cu	23.8	19.3	15.5	22.1	23.6	25.9	15.4	24.5	41.8	18.1	32.7	31.0
Zn	121	125	128	146	125	167	137	112	95.9	146	111	109
Rb	138	139	214	151	134	112	142	104	106	140	95.0	92.8
Sr	1853	945	821	954	911	1025	1499	1451	1334	1062	1411	1657
Y	32.7	34.0	30.1	33.9	33.5	35.7	32.0	27.0	26.7	33.1	23.4	25.7
Zr	549	494	518	648	510	586	588	402	419	669	355	302
Nb	50.5	49.8	58.7	63.9	48.9	54.8	21.1	46.3	42.8	64.3	58.8	45.0
Cs	3.40	3.49	10.6	4.28	3.38	1.92	3.09	2.24	2.41	3.45	3.57	3.40
Ba	1813	1656	1519	1816	1619	1787	2115	1753	1590	1956	1590	1540
La	153	156	159	174	150	155	183	123	113	169	88.3	85.1
Ce	294	301	309	339	290	300	352	236	217	334	174	166
Pr	31.6	31.9	32.6	35.9	30.7	32.2	37.8	25.7	23.4	35.7	19.5	19.1
Nd	119	122	121	138	118	123	139	97.4	89.7	137	79.5	73.5
Sm	18.2	18.5	18.7	21.2	18.2	19.3	21.2	15.4	14.0	21.4	13.2	13.0
Eu	3.53	3.48	3.18	4.07	3.49	3.96	4.12	3.37	3.08	4.20	3.40	3.25
Gd	10.8	11.0	10.8	12.3	10.9	11.7	12.6	9.76	8.54	12.5	8.63	8.85
Tb	1.41	1.44	1.39	1.58	1.46	1.52	1.52	1.21	1.11	1.59	1.14	1.11
Dy	6.32	6.65	6.13	6.97	6.59	7.01	6.69	5.53	5.09	6.92	5.38	5.14
Ho	1.06	1.12	0.98	1.12	1.11	1.19	1.11	0.95	0.85	1.11	0.89	0.87
Er	2.57	2.66	2.30	2.56	2.66	2.87	2.50	2.16	2.03	2.55	2.05	1.99
Yb	1.99	2.14	1.73	1.92	2.13	2.27	1.91	1.71	1.59	1.88	1.50	1.45
Lu	0.29	0.31	0.24	0.27	0.31	0.33	0.27	0.24	0.23	0.26	0.21	0.20
Hf	11.0	10.5	11.1	13.3	10.5	12.2	11.6	7.21	8.26	13.7	7.31	6.24
Ta	1.13	1.13	1.55	1.49	1.12	1.21	0.69	1.89	0.95	1.54	1.59	1.25
Tl	0.76	0.76	1.25	0.62	0.78	0.60	0.73	0.42	0.64	0.96	0.29	0.28
Pb	35.9	35.8	42.7	37.0	34.2	32.3	40.7	20.9	23.5	41.2	20.1	20.3
Th	23.7	27.1	41.0	29.3	27.9	22.5	28.6	15.5	16.8	25.9	10.2	13.4
U	6.09	5.29	10.73	5.98	5.51	4.51	5.69	3.04	3.36	5.45	4.29	5.33

Table 3

Present day Sr and Nd isotopic compositions of volcanic rocks from Ashikule Volcanoes.

Episode (age)	Sample	$^{87}\text{Sr}/^{86}\text{Sr}$	Error (2 σ)	$^{143}\text{Nd}/^{144}\text{Nd}$	Error (2 σ)	Ave. $^{143}\text{Nd}/^{144}\text{Nd}$	Ave. ϵNd
1 and 2 (<0.17 Ma)	ASKL-3	0.710300	0.000005	0.512272	0.000011	0.512267	-7.1
				0.512262	0.000010		
1 and 2 (<0.17 Ma)	ASKL-4	0.710295	0.000005	0.512283	0.000010	0.512283	-6.8
				0.512283	0.000012		
1 and 2 (<0.17 Ma)	518-5	0.710337	0.000005	0.512290	0.000008	0.512292	-6.6
				0.512293	0.000011		
3 (0.20-0.29 Ma)	ASKL-10	0.710463	0.000005	0.512276	0.000012	0.512265	-7.1
				0.512256	0.000010		
				0.512263	0.000016		
3 (0.20-0.29 Ma)	513-11	0.710102	0.000005	0.512275	0.000010	0.512273	-7.0
				0.512271	0.000009		
3 (0.20-0.29 Ma)	518-9	0.710353	0.000005	0.512281	0.000010	0.512279	-6.8
				0.512277	0.000011		
4 (0.46-0.60 Ma)	ASKL-7	0.710516	0.000005	0.512259	0.000012	0.512254	-7.3
				0.512250	0.000012		
4 (0.46-0.60 Ma)	ASKL-8	0.710427	0.000005	0.512265	0.000011	0.512265	-7.1
				0.512264	0.000010		
4 (0.46-0.60 Ma)	ASKL-14	0.709738	0.000005	0.512277	0.000013	0.512277	-6.9
				0.512278	0.000010		
4 (0.46-0.60 Ma)	ASKL-15	0.709696	0.000005	0.512275	0.000009	0.512277	-6.9
				0.512280	0.000011		
4 (0.46-0.60 Ma)	ASKL-16	0.709871	0.000006	0.512295	0.000009	0.512295	-6.5
4 (0.46-0.60 Ma)	515-1	0.710016	0.000005	0.512280	0.000009	0.512280	-6.8
4 (0.46-0.60 Ma)	WLK-3	0.709887	0.000005	0.512288	0.000011	0.512280	-6.8
				0.512273	0.000011		
4 (0.46-0.60 Ma)	516-2	0.709870	0.000005	0.512291	0.000011	0.512291	-6.6
5 (1.02-1.65 Ma)	ASKL-5	0.710523	0.000005	0.512265	0.000010	0.512269	-7.0
				0.512272	0.000014		
5 (1.02-1.65 Ma)	516-11	0.708887	0.000005	0.512337	0.000012	0.512336	-5.7
				0.512330	0.000010		
				0.512342	0.000014		
5 (1.02-1.65 Ma)	518-14	0.709876	0.000005	0.512291	0.000010	0.512284	-6.8
				0.512271	0.000009		
				0.512289	0.000014		
6 (2.34-2.80 Ma)	ASKL-17	0.708650	0.000005	0.512449	0.000010	0.512461	-3.3
				0.512473	0.000013		
6 (2.34-2.80 Ma)	ASKL-18	0.707490	0.000005	0.512487	0.000010	0.512472	-3.1
				0.512461	0.000011		
				0.512469	0.000011		

 $^{143}\text{Nd}/^{144}\text{Nd}$ of chondritic uniform reservoir (CHUR) (0.512630; Bouvier et al., 2008) is used to calculate ϵNd .